

A Global Fit of Non-Relativistic Effective Dark Matter Operators Including Solar Neutrinos

N. P. Avis Kozar ^{1,2}, Pat Scott ⁴ and A. C. Vincent ^{1,2,3}

¹*Department of Physics, Engineering Physics, and Astronomy, Queen's University, Bader Lane, Kingston, Canada*

²*Arthur B. McDonald Canadian Astroparticle Physics Research Institute, Queen's University, Bader Lane, Kingston, Canada*

³*Perimeter Institute for Theoretical Physics, Caroline Street North, Waterloo, Canada*

⁴*Quantum Brilliance Pty Ltd, The Australian National University, Daley Road, Acton ACT 2601, Australia*

(Dated: February 6, 2025)

We perform a global fit of dark matter interactions with nucleons using a non-relativistic effective operator description, considering both direct detection and neutrino data. We examine the impact of combining the direct detection experiments CDMSlite, CRESST-II, CRESST-III, DarkSide-50, DarkSide-50-S2-Only, LUX, LZ, PandaX-II, PandaX-4T, PICO-2L, PICO-60, SIMPLE, XENON100, and XENON1T along with neutrino data from IceCube, ANTARES, DeepCore, and Super-Kamiokande. While current neutrino telescope data lead to increased sensitivity compared to underground nuclear scattering experiments for dark matter masses above 100 GeV, our future projections show that the next generation of underground experiments will significantly outpace solar searches for most dark matter-nucleon elastic scattering interactions.

I. INTRODUCTION

Observations across a range of cosmic scales, from galactic rotation curves [1] to the angular power spectrum of the cosmic microwave background [2], point to a large component of weakly-interacting, cold dark matter (DM). The nature of DM remains unknown. If it is a weakly-interacting particle in the \sim GeV–TeV range, it could leave an imprint in direct detection (DD) experiments, which search for energy deposition from DM elastically scattering with target nuclei. Thus far, no detection has been confirmed, and increasingly strong limits have been placed on DM interacting with nucleons via a constant spin dependent (SD) or spin independent (SI) coupling, respectively parametrized via their cross section with nucleons σ_{SI} and σ_{SD} . These limits span many orders of magnitude in mass and cross section; see e.g. [3–5].

Possible microphysical interactions extend well beyond σ_{SI} and σ_{SD} . Over the past decade, a formalism has been developed to parametrise the set of non-relativistic effective interactions in the low-energy limit of a generic dark sector model [6–8]. By decomposing possible interaction Hamiltonian terms into products of available Hermitian operators that may couple DM to nucleons, one finds cross sections that scale with powers of the relative DM-nucleus velocity, transferred momentum, or particle spins, which in turn give rise to different phenomenology. The 14 operators that make up the non-relativistic effective operator (NREO) formalism have now become standard; see e.g. [9] for a full description, including how they may arise from a relativistic theory.

Any interaction between DM and nuclei in the lab also implies interactions in celestial bodies such as stars. Should DM have some novel interaction with baryonic matter, then through kinematic scattering with nuclei in the Sun the DM could become gravitationally bound to it. This may lead to a neutrino signal if the DM can

self-annihilate to Standard Model (SM) final states. Extensive searches for such a signal have been performed by neutrino telescopes including Super-Kamiokande [10], ANTARES [11, 12] and IceCube [13–17]. These are presented as constraints on the DM-nucleus scattering cross section σ_{SI} , σ_{SD} since in a steady state, the annihilation rate is equal to the capture rate, proportional to $\sigma_{\chi n}$. It is important to note that these constraints are strongly dependent on the annihilation channel, each of which yields a specific spectrum and flux of neutrinos.

The Sun and underground experiments probe different kinematic regimes: DD is by design most sensitive to high-velocity and high momentum-transfer interactions, and benefits from the A^2 coherent enhancement of scattering with heavy nuclei; the Sun, primarily composed of hydrogen, presents a large target for spin-dependent scattering, and can more readily sample the low-velocity tail of the dark matter phase space distribution. These two methods are thus complementary in the types of interactions they may see.

Previous work has examined the effect of non-constant DM-nucleus interactions on the capture rate of dark matter in the Sun. Ref. [18] obtained capture rates for generic spin-dependent and independent interactions that scale with the relative velocity and momentum transfer. Ref. [19] computed cross sections and capture rates in the context of the NREO formalism, and found parametrizations for the effective nuclear response (or *form factor*) for the most abundant elements in the Sun. In Ref. [20], these were used to place constraints on 28 different coupling constants using one year of IceCube 79-string data, as well as reported data from Super-Kamiokande. Ref [21] further constrained the effective theory of *inelastic* effective interactions, and complementarity between experiments in the NREO framework was examined in Ref. [22].

In contrast with [22] where the authors looked to emphasize potentially incorrect conclusions drawn from the comparison of specific models with individual interaction

limits, here we wish to investigate a global analysis of NREOs. As a result we do not pick specific high energy theories corresponding to a subset of interaction types, but rather investigate the relative contributions to each interaction from the experiments considered. While this work included visual comparison of solar neutrino constraints with direct detection results, no self-consistent combination of likelihoods from both sectors has been considered in the context of NREO searches. That is to say, self-consistently including common nuisance factors in the computation of likelihoods across all experiments and between direct detection and solar neutrino constraints. Further, neutrino data included in previous analyses has been limited to only a small fraction of the more than ten years over which IceCube has operated.

In this work, we thus implement solar capture and direct detection calculations in the NREO interaction formalism into the Global and Modular Beyond-the-Standard-Model Inference Tool (GAMBIT) [23], and perform a global fit of this parameter space including possible nuisance parameters that both sectors may have in common. By combining likelihoods before reporting constraints, we ensure self-consistency, and may access parameter space that is not covered by simply overlaying constraints from individual experiments [24]

We make use of the DD experiments included in GAMBIT. These include liquid noble gas detectors, superheated fluorine experiments, and cryogenic crystal experiments: CDMSlite [25], CRESST-II [26], CRESST-III [27], DarkSide-50 [28], DarkSide-50-S2-Only [29], LUX [30], LZ [31], PandaX-II [32, 33], PandaX-4T [34], PICO-2L [35], PICO-60 [36–38], SIMPLE [39], XENON100 [40], and XENON1T [41]. The solar constraints come from IceCube [13–15, 17], ANTARES [42], Super-Kamiokande [10], and DeepCore [43] neutrino data. Of particular importance, IceCube has recently shown preliminary constraints on dark matter capture and annihilation in the Sun [17] using 9 years of 86-string data, which we recast here. We will furthermore show projected sensitivities for the some of the most significant planned experiments: DARWIN [44], PICO-500 [45], and a combined set of planned future neutrino experiments.

The DD constraints largely make use of work developed in the context of prior GAMBIT publications. Specifically, Ref. [46] included a combination of DD and IC79 constraints on relativistic effective operators; we refer the reader to that reference for details on the DD implementation. Here, we will rather focus on the novel implementation of the solar capture rates computed within the NREO formalism, their interplay with DD experiments, and the future of such combined searches for dark matter.

This article is organized as follows: in Sec. II, we review the NREOs formalism, and in Sec. III we show how capture of DM in the Sun is computed. Sec. IV covers the details of the software implementation in the Capt'n General code, designed to calculate solar DM capture rates using the NREO formalism, and how Capt'n General in-

terfaces with GAMBIT. Sec. V contains our main results, and finally Sec. VI summarizes the work of this paper and future prospects to expand on this work. The GAMBIT scan outputs and script for reproducing the plots found in this paper can be found in a Zenodo dataset [47].

II. NON-RELATIVISTIC EFFECTIVE OPERATOR DARK MATTER

We make use of NREOs following the convention from [19], which are developed from [8]. This work focuses on the use of NREOs as a method to describe elastic interactions between DM from the Milky Way (MW) halo and nuclei in the Sun. The operators are constructed to describe DM interactions mediated by a massive particle of spin-zero or spin-one. These effective operators are constructed from five Hermitian operators that obey Galilean invariance. These are the transferred momentum $i\hat{\mathbf{q}}$, the relative transverse velocity $\hat{\mathbf{v}}^\perp$, the nucleon spin $\hat{\mathbf{S}}_N$, the DM spin $\hat{\mathbf{S}}_\chi$, and the identity $\mathbb{1}_{\chi N}$ in the DM-nucleon space:

$$\mathbb{1}_{\chi N} , i\hat{\mathbf{q}} , \hat{\mathbf{v}}^\perp , \hat{\mathbf{S}}_\chi , \hat{\mathbf{S}}_N . \quad (1)$$

The quantity $\hat{\mathbf{v}}^\perp = \hat{\mathbf{v}} + \hat{\mathbf{q}}/(2\mu_N)$ is defined using the relative velocity between the nucleon and incoming DM particle $\hat{\mathbf{v}}$, and is constructed such that $\hat{\mathbf{q}} \cdot \hat{\mathbf{v}}^\perp = 0$, ensuring linear independence.

The interaction operators that can be constructed from the basis (1) are shown in Tab. I. Further, the second operator $\hat{\mathcal{O}}_2 = (\hat{\mathbf{v}}^\perp)^2$ will be omitted in following with [48] as it cannot be leading order in a non-relativistic limit of a relativistic model of DM interactions. As we are interested in DM in the galactic halo, the DM has velocities below the escape velocity ($v_{\text{esc}} = 544 \text{ km s}^{-1}$ [49]), so such non-relativistic limits are safe to consider. It is worth noting that the first ($\hat{\mathcal{O}}_1$) and fourth ($\hat{\mathcal{O}}_4$) operators respectively correspond to the standard, constant SI and SD interactions.

Generically, the low-energy limit of an effective DM-SM interaction can be parameterised as a linear combination of the operators in Tab. I:

$$\hat{\mathcal{H}}(\mathbf{r}) = \sum_{\tau=0,1} \sum_{k=1}^{15} c_k^\tau \hat{\mathcal{O}}_k(\mathbf{r}) t^\tau , \quad (2)$$

where t^τ represents the coupling to weak isospin: $t^0 = \mathbb{1}$ represents isoscalar couplings, and $t^1 = \tau_3$ (the third Pauli matrix) for isovector couplings. The couplings can be projected onto the basis of protons or neutrons: $c_k^{p/n} = (c_k^0 \pm c_k^1)/2$.

Each DM-nucleon interaction operator couples to a different combination of states in the basis of the *nucleus*. For example $\hat{\mathcal{O}}_3$ contains the nucleon spin $\hat{\mathbf{S}}_N$, but does not couple to the total nucleus spin, but to the spin-orbit interaction. This yields nonzero effective couplings

$\widehat{\mathcal{O}}_1 = \mathbb{1}_{\chi N}$	$\widehat{\mathcal{O}}_9 = i\widehat{\mathbf{S}}_\chi \cdot \left(\widehat{\mathbf{S}}_N \times \frac{\widehat{\mathbf{q}}}{m_N} \right)$
$\widehat{\mathcal{O}}_3 = i\widehat{\mathbf{S}}_N \cdot \left(\frac{\widehat{\mathbf{q}}}{m_N} \times \widehat{\mathbf{v}}^\perp \right)$	$\widehat{\mathcal{O}}_{10} = i\widehat{\mathbf{S}}_N \cdot \frac{\widehat{\mathbf{q}}}{m_N}$
$\widehat{\mathcal{O}}_4 = \widehat{\mathbf{S}}_\chi \cdot \widehat{\mathbf{S}}_N$	$\widehat{\mathcal{O}}_{11} = i\widehat{\mathbf{S}}_\chi \cdot \frac{\widehat{\mathbf{q}}}{m_N}$
$\widehat{\mathcal{O}}_5 = i\widehat{\mathbf{S}}_\chi \cdot \left(\frac{\widehat{\mathbf{q}}}{m_N} \times \widehat{\mathbf{v}}^\perp \right)$	$\widehat{\mathcal{O}}_{12} = \widehat{\mathbf{S}}_\chi \cdot \left(\widehat{\mathbf{S}}_N \times \widehat{\mathbf{v}}^\perp \right)$
$\widehat{\mathcal{O}}_6 = \left(\widehat{\mathbf{S}}_\chi \cdot \frac{\widehat{\mathbf{q}}}{m_N} \right) \left(\widehat{\mathbf{S}}_N \cdot \frac{\widehat{\mathbf{q}}}{m_N} \right)$	$\widehat{\mathcal{O}}_{13} = i \left(\widehat{\mathbf{S}}_\chi \cdot \widehat{\mathbf{v}}^\perp \right) \left(\widehat{\mathbf{S}}_N \cdot \frac{\widehat{\mathbf{q}}}{m_N} \right)$
$\widehat{\mathcal{O}}_7 = \widehat{\mathbf{S}}_N \cdot \widehat{\mathbf{v}}^\perp$	$\widehat{\mathcal{O}}_{14} = i \left(\widehat{\mathbf{S}}_\chi \cdot \frac{\widehat{\mathbf{q}}}{m_N} \right) \left(\widehat{\mathbf{S}}_N \cdot \widehat{\mathbf{v}}^\perp \right)$
$\widehat{\mathcal{O}}_8 = \widehat{\mathbf{S}}_\chi \cdot \widehat{\mathbf{v}}^\perp$	$\widehat{\mathcal{O}}_{15} = - \left(\widehat{\mathbf{S}}_\chi \cdot \frac{\widehat{\mathbf{q}}}{m_N} \right) \left[\left(\widehat{\mathbf{S}}_N \times \widehat{\mathbf{v}}^\perp \right) \cdot \frac{\widehat{\mathbf{q}}}{m_N} \right]$

TABLE I. All fourteen linearly independent NREOs, adopted from [19].

between this ‘‘spin-dependent’’ particle and e.g. the spin-zero ^{40}Ar nucleus.

As an example of how such operators could arise, we may look at $\widehat{\mathcal{O}}_{10}$, which could arise from a parity-violating DM-quark interaction mediated by a heavy scalar [9]:

$$\mathcal{L} \supset \lambda_1 \phi \bar{\chi} \chi - i h_2 \phi \bar{q} \gamma^5 q \rightarrow \widehat{\mathcal{H}} \supset (c_{10}^0 t^0 + c_{10}^1 t^1) \widehat{\mathcal{O}}_{10}, \quad (3)$$

in this case $\widehat{\mathcal{O}}_{10}$ is the leading operator contributing to this interaction. Here λ_1 and h_2 are coupling parameters in the EFT Lagrangian, χ is the DM, q are quarks, ϕ is a scalar mediator between the DM and quarks.

The DM-nucleus scattering cross section can be factored into a DM response function $R^{\tau\tau'}$, which depends on the combination of couplings, and a nuclear response function $W^{\tau\tau'}$.

The DM response functions take a general form:

$$R^{\tau\tau'} \left(\widehat{\mathbf{v}}_{\text{T}}^{\perp 2}, \frac{\widehat{\mathbf{q}}^2}{m_N^2}, \left\{ c_i^\tau c_j^{\tau'} \right\} \right) = \sum_{n=0}^1 \sum_{m=0}^2 A_{n,m} \left(\widehat{\mathbf{v}}_{\text{T}}^{\perp 2} \right)^n \left(\frac{\widehat{\mathbf{q}}^2}{m_N^2} \right)^m \left\{ c_i^\tau c_j^{\tau'} \right\}_{n,m}, \quad (4)$$

where they generically appear as quadratic combinations of the velocity (indexed by n) and transferred momentum (indexed by m) with prefactors $A_{n,m}$ and pairs of coupling constants. The coupling constant pairs are bounded by curly braces, where each pair is associated with a unique combination of velocity and momentum powers (n, m) , and each pair may ($i = j$) or may not ($i \neq j$) correspond to the same operator index. The specific form for all DM response functions can be found in Appendix A of [19]. The nuclear response functions that we use were computed using nuclear shell models and tabulated in Ref. [19]. These are fitted to the general form:

$$W^{\tau\tau'}(y) = \exp(-2Dy) \sum_{i=0}^6 A_i^{\tau\tau'} y^i, \quad (5)$$

where the exponential may ($D = 1$, not hydrogen) or may not ($D = 0$, hydrogen) contribute to a given function

depending on which isotope is being calculated, and the coefficients $A_i^{\tau\tau'}$ corresponding to each power of y and each isospin index (τ, τ') must be computed separately for each isotope.

The parameter y is defined as:

$$y = \left(\frac{bq}{2} \right)^2, \quad (6)$$

and b is a length parameter corresponding to the scale of the nucleus:

$$b = \sqrt{\frac{41.467}{45A^{-\frac{1}{3}} - 25A^{-\frac{2}{3}}} \text{ fm}}, \quad (7)$$

where A is the atomic mass number of the isotope.

While the couplings c_i^τ are in principle derived from a UV-complete theory, they are difficult to compare directly with other DM search results. We may define an effective cross section (as in e.g. [50]):

$$\sigma_N = \frac{(c_i^0 \mu_p)^2}{4\pi}, \quad (8)$$

where μ_p is the proton-DM reduced mass, and we consider an isoscalar ($c_i^0 \neq 0, c_i^1 = 0$) interaction, making use of $c_i^p = (c_i^0 + c_i^1)/2$. While isospin violation has been invoked in many contexts (mainly to remove constraints from specific experiments), we limit ourselves to isospin-conserving interactions, as it is a minimal assumption on how the dark sector couples to quarks. On the practical side, it means one fewer free parameter per operator. In the case of a constant cross section these directly correspond to the constant SI ($\widehat{\mathcal{O}}_1$) and SD ($\widehat{\mathcal{O}}_4$) interactions, though to match with the typical definition of SD the effective cross section expression in (8) is multiplied by 3/16 [48, 51]. It is worth emphasizing that Eq. (8) loses its immediate significance for velocity or momentum-dependent interactions.

III. STELLAR CAPTURE AND ANNIHILATION

Below, we describe the process of gravitational capture of halo DM by the Sun. We take the DM to follow

a Maxwell-Boltzmann distribution. In the frame of the Sun [52]:

$$f_{\odot}(u) = \left(\frac{3}{2}\right)^{3/2} \frac{4\rho_{\chi}u^2}{\pi^{1/2}m_{\chi}u_0^3} \exp\left(-\frac{3(u_{\odot}^2 + u^2)}{2u_0^2}\right) \frac{\sinh(3uu_{\odot}/u_0^2)}{3uu_{\odot}/u_0^2}, \quad (9)$$

where ρ_{χ} and m_{χ} are the DM density and mass, u is the DM velocity, u_0 is the velocity dispersion, and u_{\odot} is the Sun's velocity.

The particle can be scattered elastically to a velocity below the local escape velocity, allowing it to be gravitationally bound to the Sun. The capture rate can be written as an integral over the Sun's radius R_{\odot} and the second over the DM velocity distribution [53]:

$$C = 4\pi \int_0^{R_{\odot}} r^2 dr \int_0^{\infty} \frac{f(u)}{u} w(r) \Omega_v^-(w(r)) du, \quad (10)$$

where $\Omega_v^-(w(r))$ is the rate at which DM is scattered from speed $w(r) = \sqrt{u^2 + v_{esc}(r)^2}$ below the local escape velocity $v_{esc}(r)$:

$$\Omega_v^-(w) = \sum_i n_i w \Theta\left(\frac{\mu_i}{\mu_{\pm,i}^2} - \frac{u^2}{w^2}\right) \int_{E_k u^2/w^2}^{E_k \mu_i/\mu_{\pm,i}^2} dE_R \frac{d\sigma_i}{dE_R}(w^2, q^2). \quad (11)$$

The sum is over the different isotopes found in the Sun, where n_i is the i^{th} isotope's abundance as a function of the radius, $E_k = m_{\chi}w^2/2$ is the kinetic energy of the DM particle, and

$$\mu_i \equiv \frac{m_{\chi}}{m_i}, \quad \mu_{\pm,i} \equiv \frac{\mu_i \pm 1}{2}. \quad (12)$$

Ω_v^- depends on the differential cross section $d\sigma/dE_R$.

The integrals in Eqs. 10-11 can be factored into terms of the form (polynomial in y) e^{-y} which have solutions proportional to gamma functions and are detailed in Ref. [18]. By performing this factorisation, and gathering terms by order in y , where $y \propto q^2$ is defined in Eq. 6, the integral (11) can be sped up significantly.

The geometric limit $\sigma_{\max} = \pi R_{\odot}^2(t)$ for which the star captures all DM it encounters leads to a maximum capture rate [18]:

$$\begin{aligned} C_{\max}(t) &= \pi R_{\odot}^2(t) \int_0^{\infty} \frac{f_{\odot}(u)}{u} w^2(u, R_{\odot}) du \\ &= \frac{1}{3} \pi \frac{\rho_{\chi}}{m_{\chi}} R_{\odot}^2(t) \left(e^{-\frac{3}{2} \frac{u_{\odot}^2}{u_0^2}} \sqrt{\frac{6}{\pi}} u_0 \right. \\ &\quad \left. + \frac{6G_N M_{\odot} + R_{\odot}(u_0^2 + 3u_{\odot}^2)}{R_{\odot} u_0} \text{Erf}\left[\sqrt{\frac{3}{2}} \frac{u_{\odot}}{u_0}\right] \right), \end{aligned} \quad (13)$$

Where G_N is Newton's gravitational constant. Eq. (13) includes gravitational focusing. The overall capture rate is then the minimum of Eq. (10) and Eq. (13).

A. Dark Matter in the Sun

For DM masses above approximately $m_{\chi} \simeq 4$ GeV, evaporation rapidly becomes negligible [54]. As here our most relevant constraints from annihilating DM only exist at $\mathcal{O}(100 \text{ GeV})$, this evaporation effect can be safely ignored. In addition, for the cross sections considered here, we have checked that the capture and annihilation rates in the Sun will have equilibrated by now. The annihilation rate is therefore equal to the capture rate, and thus proportional to the DM-nucleon scattering cross section. Annihilation to any SM product will eventually yield a neutrino flux. We will examine a few representative channels: $\chi\chi \rightarrow b\bar{b}$, W^+W^- and $\tau^+\tau^-$. Once neutrinos are produced, they will quickly escape the core of the Sun and can be detected at Earth-based observatories including IceCube, ANTARES, DeepCore, and Super-Kamiokande [11, 13–15, 43, 55].

IV. METHODS

A. GAMBIT

Our global scan uses GAMBIT [23], a global fitting package that allows users to specify models, perform likelihood calculations based on physical observables, and scan large parameter spaces with state-of-the-art scanners. GAMBIT has the ability to compute likelihoods directly, but also to “backend” existing public code such as DarkSUSY [56, 57], DDCalc [58, 59] and Capt'n General [60]. GAMBIT is publicly available at <https://gambitbsm.org>. For this work, we used a modified version of 2.3.1.

GAMBIT is made of several modules, each corresponding to a class of observables like DecayBit [61] and DarkBit [58] which handle decay rates and DM physics respectively, or computations like the ScannerBit module [62], which is designed to coordinate the exploration of the likelihood parameter space through the use of Markov Chain Monte Carlo (MCMC) (GReAT [63] and T-Walk [62]), nested sampling (MultiNest [64]), or differential evolution (DE) (Diver [62], which we use for this work) packages. GAMBIT is designed modularly such that observables can be used in arbitrary functions defined using genericized dependencies and output capabilities. The functions of GAMBIT can request an arbitrary number and variety of dependencies. Each function then has an output capability, which further functions can use as input dependencies. In addition, GAMBIT can also make use of external code packages called backends for capability calculation. Capt'n General is one of these backends.

This structure allows GAMBIT to determine a call order of functions to calculate likelihoods from desired observables using as many intermediate steps as required. This dependency resolver constructs an acyclic graph to organize the function calls such that the capabilities are properly passed down the resolved tree to calculate likelihoods. In addition, any ambiguous call order is resolved intelligently by making faster function calls first such that points can be invalidated by quicker likelihood calculations before slower ones. With a call order established, ScannerBit controls the exploration of the parameter space according to the selected scanning algorithm. Our scans will use DarkBit, as well as SpecBit and DecayBit to read in SM inputs and generate decay rates for the catalogue of annihilation products.

For this work, the GAMBIT front end required additions to accommodate the NREO parametrization. This included incorporating the couplings to the inbuilt DDCalc coupling dependencies, and creating a catalogue of particles that can be produced in DM annihilation.

B. Direct Detection Likelihoods

The DD experiments are handled by GAMBIT through the use of the DarkBit module [58], which handles the calculation of event rates in each experiment from the input couplings through the use of DDCalc [58, 59].

DDCalc is a backend for recasting direct search limits. It calculates the predicted rates and likelihoods for a variety of experiments, given an input dark matter and halo model. Data is compared with these predictions using a binned Poisson likelihood. DDCalc models experimental backgrounds when made available by each collaboration; otherwise it computes a one-sided likelihood that can be used for exclusion (disfavouring models that predict larger event numbers than observed), but cannot identify a preferred signal. As of DDCalc v2.0 [59], the code allows for the use of NREOs directly, and incorporates the nuclear response functions computed in [48] necessary to evaluate Eq. (5) in the context of DD experiments. As stated earlier, we use the likelihoods for CDMSlite [25], CRESST-II [26], CRESST-III [27], DarkSide-50 [28], DarkSide-50-S2-Only [29], LUX [30], LZ [31], PandaX-II [32, 33], PandaX-4T [34], PICO-2L [35], PICO-60 [36–38], SIMPLE [39], XENON100 [40], and XENON1T [41]. Details of how the results of each experimental analysis is recast can be found in Appendix A of Ref. [59].

C. Solar Capture

We compute the solar capture rate using the Capt'n General code [60]. Capt'n General is written in Fortran 90. It makes use of a set of DM halo parameters, a solar model with elemental abundances, and a set of DM parameters, to calculate the DM capture rate in the Sun. It

is written to interface as an external library in software such as GAMBIT or MESA. The first version of Capt'n General parametrised non-constant DM-nucleus interactions using the formalism of [18], where the DM-nucleus interactions were scaled with momentum and velocity, i.e. $\sigma = \sigma_0(v/v_0)^{2n}$ or $\sigma = \sigma_0(q/q_0)^{2n}$, where v_0 and q_0 are arbitrary reference values. We extended Capt'n General to make use of the NREO formalism as discussed in Sec. II [60].¹

A key part of the software uses Generalized Form Factor Integrals (GFFIs) to calculate integrals of the form²

$$GFFI = \int_{y_{\min}}^{y_{\max}} y^n e^{-D2y} dy. \quad (14)$$

as in Eqn. (11), with $y_{\min} = b^2 u^2 m_i m_\chi / 4$ and $y_{\max} = b^2 w^2 m_\chi^2 / 4 \mu_{+,i}^2$. For each operator, the dark matter response function and the nuclear form factors come with sums over powers of y . Capt'n General first groups integrals into powers of y , evaluates the results of Eq. (14), and performs the sums in Eqs. (4) and (5).

When the target is hydrogen ($D = 1$),

$$GFFI_{n \neq 0, H} = \begin{cases} \frac{1}{1+n} \left(\frac{b^2 w^2 m_i m_\chi}{4} \right)^{n+1} \left[\left(\frac{\mu}{\mu_{+,i}} \right)^{n+1} - \left(\frac{u}{w} \right)^{n+1} \right] & (n \neq -1) \\ \ln \left(\frac{\mu}{\mu_{+,i}} \frac{w^2}{u^2} \right) & (n = -1). \end{cases}, \quad (15)$$

When $D = 1$,

$$GFFI_{n \neq 0, i \neq H} = \frac{1}{2^{n+1}} \left[\Gamma \left(1 + n, \frac{b^2 u^2 m_i m_\chi}{2} \right) - \Gamma \left(1 + n, \frac{b^2 w^2 m_\chi^2}{2 \mu_{+,i}^2} \right) \right], \quad (16)$$

where $\Gamma(m, x)$ is the (upper) incomplete gamma function.

Once integrals over $y \propto q^2$ have been performed, integrals over velocity are done numerically using a QUADPACK [56, 65], after which the integral over the volume of the star is performed with trapezoidal integration. We precompute a set of prefactors that each are a sum of all calculated constants from their respective GFFI velocity and momentum combinations. This set of prefactors can then be used to make the minimum number of calls to the numerical integration routine to complete the velocity (u) integral of Eqn. (10), allowing the code to entirely skip some calls depending on which prefactors end up being zero.

¹ github.com/aaronvincent/captngen

² The actual implementation is based on the variable E_R rather than y , so the exact form of the GFFI in the code more closely follows Ref. [18]. Because of this, the GFFI results presented here each differ by a constant factor.

Capt'n General is implemented as a backend to GAMBIT, and is called once per likelihood evaluation. The current release of GAMBIT 2.3.1 includes event-level neutrino likelihoods from the 3-year 79-string IceCube (IC79) data [13, 15] via nlike [14], with neutrino spectra generated and propagated to Earth by DarkSUSY [56, 57]. We supplement these with the most recently-presented IceCube analysis using 8 years of data and the full 86-string detector [66] at masses above 300 GeV, and use the older IC79 dataset for masses below. These were presented as 90% limits on the spin-independent DM-nucleon scattering cross section as a function of DM mass. To incorporate the [66] results, we map their constraints on a constant, spin-dependent dark matter-nucleon cross section onto a constraint on the capture rate using Capt'n General. This allows us to set limits for any arbitrary combination of NREO operators and couplings. In the same way, we also include recently-presented ANTARES [42] limits, and the most recent DeepCore [43] and Super-Kamiokande [10] limits.

D. Differential Evolution Scanner

We employ the Diver [62] scanner, a DE algorithm for parameter space sampling. Ref. [62, 67] showed that Diver is much more efficient than a range of other algorithms at finding features in parameter space, with the drawback of not yielding a posterior likelihood distribution. This will not be an issue, as we will present results in terms of frequentist profile likelihoods.

The DE algorithm uses a set of points placed in the parameter space which are used to map the likelihood. This process occurs in three steps: mutation, crossover, and selection.

DE starts from an initial random population of points. The first step is mutation: for each point three other points are selected randomly, two of which are used to create a donor vector and applied to the third point with a scaling factor. In the second step (crossover) the donor vector is mixed with the original point's vector to produce a trial vector. This is done by stepping through each component of the trial vector and randomly choosing either the original's or the donor's component. After each component is chosen, if this trial vector mixture is identical to the original point then a random component is chosen to be switched for the donor's. In the third step (selection) the original point's and trial vector's likelihood are compared, and the one with the better value is retained for the next set of initial points – if the likelihood is equal, the trial vector is chosen to allow the algorithm to explore flat regions [62].

DE is useful here as it is focused on mapping the contours of the parameter space being scanned, rather than identifying global minima. As Diver only accepts updated points that improve the population's likelihood, the algorithm tends to converge faster than alternatives that can accept inferior points based on random chance

such as MCMCs.

Varying all NREO operators simultaneously would not yield much constraining power. We separate the GAMBIT scan into fourteen sets of parameter space scans of each isoscalar NREO in Tab. I, where each isoscalar operator had three scan versions depending on annihilation channel: one with annihilation to $b\bar{b}$ which yields a soft neutrino spectrum, a second with annihilation to W^+W^- (harder), and a third with annihilation to $\tau^+\tau^-$ (hardest). Annihilation to other final states, or a combination of these, would yield constraints intermediate between these cases, except for the direct annihilation to neutrinos.³ Results for these final states are available in IceCube [13–15, 17] analyses used here. Including isovector couplings, equivalent to varying the ratio of proton-to-neutron couplings, would change the relative constraining power of direct detection experiments examined here (to see this interplay, see e.g. [22, 69]). To avoid the additional computational time associated with this extra parameter in each model, we restrict ourselves to isoscalar models (equal coupling to protons and neutrons). We fix the annihilation cross-section to $3 \times 10^{-26} \text{ cm}^3 \text{ s}^{-1}$. In each of the forty-two individual scans the DM mass was allowed to vary from 1 GeV to 10 TeV with a log-flat prior. In addition, we chose each scan's coupling range such that the scans captured the region in which the 90% CL resided, with the beginning and end points chosen by first referencing a coarser and quicker initial scan. We show these coupling parameter ranges in the first section of Tab. II. We performed each of these scans using a population of 10^4 , and a convergence threshold of 10^{-3} in Diver [62].

In addition, each scan also included three nuisance parameters quantifying the DM velocity distribution: the halo velocity dispersion v_0 , the galactic escape velocity v_{esc} and the Sun's galactic rotational velocity v_{rot} . We set the local dark matter density to 0.5 GeV cm^{-3} , and did not vary it, as it is completely degenerate with the (square of the) couplings. We allowed each nuisance parameter to vary with a gaussian prior with central values and widths informed by Refs. [70] and [71], as used in Ref. [46]. These are shown in the second section of Tab. II. We processed the resulting Diver scans using Pippi [72] and plotted the results using Matplotlib [73] and adjustText [74].

³ Indeed, direct annihilation to $\bar{\nu}\nu$ would yield the strongest constraints. However, models that predict a strong enough coupling to quarks (necessary for capture), while retaining a large annihilation rate directly to neutrinos, would necessitate some tuning. Even in the case of e.g. Kaluza Klein dark matter which yields such a channel, the dominant neutrino flux comes from charged τ decay [68].

Coupling parameters (GeV ⁻²)	
$\log_{10}(c_1^0)$	(-10, -6)
$\log_{10}(c_3^0)$	(-6, -3)
$\log_{10}(c_4^0)$	(-8, -3)
$\log_{10}(c_5^0)$	(-5, -2)
$\log_{10}(c_6^0)$	(-5, -1)
$\log_{10}(c_7^0)$	(-4, -1)
$\log_{10}(c_8^0)$	(-6, -4)
$\log_{10}(c_9^0)$	(-6, -1)
$\log_{10}(c_{10}^0)$	(-6, -2)
$\log_{10}(c_{11}^0)$	(-9, -5)
$\log_{10}(c_{12}^0)$	(-8, -4)
$\log_{10}(c_{13}^0)$	(-5, -1)
$\log_{10}(c_{14}^0)$	(-3, 1)
$\log_{10}(c_{15}^0)$	(-5, -2)

Common model parameters	
$\log_{10}(m_{\text{dm}})$ (GeV)	(0, 4)
ρ_0 (GeV cm ⁻³)	0.5
v_0 (km sec ⁻¹)	(216, 264)
v_{rot} (km sec ⁻¹)	(216, 264)
v_{esc} (km sec ⁻¹)	(453, 603)

TABLE II. Table of parameters used in the global Diver scans. Each individual scan is over a single coupling, while every scan includes the common parameters listed in the lower portion of the table. The dark matter mass (m_{dm}) and couplings (c_i^0) have log-flat priors, and the halo parameters (v_0 , v_{rot} , and v_{esc}) have Gaussian priors, where the ranges indicate the $3\text{-}\sigma$ ranges of these values. The halo parameters have the same range as used in [46], where the ranges of v_0 , v_{rot} and v_{esc} are from [70] and [71] respectively.

V. RESULTS

The results are presented in Figs. 1, 2, and 3 as profiled likelihoods, where we show 90% CL contours, and the black (low-likelihood) regions are excluded. We present three panels for each of the isoscalar couplings corresponding to the $b\bar{b}$, W^+W^- , and $\tau^+\tau^-$ annihilation channels. We show the 90% CL contour contributed by individual experiments to the total likelihood, which also has its own 90% CL contour shown. For clarity, we only show the constituent 90% CL contours for experiments that dominate in contribution to the total likelihood.

We show neutrino telescope constraints from IC79, ANTARES, IceCube (2022), DeepCore, and Super-Kamiokande. Note that the IC79 and IceCube (2022) samples have overlap and are thus not independent. However, the IceCube (2022) analysis *does not* extend below 300 GeV. Therefore, we include the IC79 results in the total log-likelihood only below 300 GeV, and the IceCube (2022) results only above 300 GeV.

In the main text, we will present constraints on c_1^0 and c_4^0 , which respectively yield the SI and SD constant cross sections, in addition to c_7^0 , c_{10}^0 and c_{11}^0 , which illustrate the different ways in which DD and neutrino telescopes complement each other. The full results for the 14 op-

erators shown in Tab. I are presented in Appendix A, including individual likelihood contributions of *every* experiment.

The results of the scans for c_1^0 and c_4^0 are shown in Fig. 1, plotted using both the coupling and the effective cross section as expressed in Eq. (8).

Not unexpectedly, direct detection experiments dominate spin-independent limits due to the coherent A^2 enhancement of the cross section, whereas neutrino telescopes remain competitive in spin-dependent searches for some channels at higher DM masses. Harder spectra (W^+W^- and $\tau^+\tau^-$) yield more competitive results.

The likelihoods are fairly flat outside the excluded region, indicating the absence of a preferred region of parameter space.

Some of the strongest constraints from neutrino telescopes are on the $\hat{\mathcal{O}}_7$ operator, shown in the top panels of Fig. 2. $\hat{\mathcal{O}}_7$ is spin-dependent and velocity-suppressed. It is unclear however whether such an operator can be the dominant operator in a full theory. It can occur in the presence of a parity-violating vector interaction, but this also comes in a linear combination with $\hat{\mathcal{O}}_9$ operator [9], which does not couple to the total nucleus spin, and therefore is more readily accessible at direct detection experiments.

Results for ($\hat{\mathcal{O}}_{10} = i\hat{\mathbf{S}}_{\text{N}} \cdot \frac{\hat{\mathbf{q}}}{m_{\text{N}}}$) are also shown in Fig. 2. This operator shares some similarity to the SD constraints in Fig. 1 and Fig. 8, in that the neutrino constraints are competitive with, but not dominant over other DD constraints. Finally, we show results for ($\hat{\mathcal{O}}_{11} = i\hat{\mathbf{S}}_{\text{X}} \cdot \frac{\hat{\mathbf{q}}}{m_{\text{N}}}$) in Fig. 3, whose spin-independent, momentum-suppressed cross section leads DD experiments to dominate constraints.

A number of operators, including $\hat{\mathcal{O}}_{10}$ and $\hat{\mathcal{O}}_{11}$, show a higher-likelihood (brighter colour) region just below the exclusion lines. These are driven by xenon experiments, and LZ in particular, which see downward fluctuations at lower recoil energies with respect to the background model. This results in a slightly better fit for dark matter models that predict a rise in recoil rates with energy. These higher-likelihood regions are not significant, however, as can be seen from the profile likelihood ratio colour scale.

To explain the relative power of solar versus direct detection data, we may look at how each of these operators couple to nuclei. As stated above, $\hat{\mathcal{O}}_7$ and $\hat{\mathcal{O}}_{10}$ depend on the nuclear spin, so are more difficult to reach by experiments with no spin-dependent sensitivity. $\hat{\mathcal{O}}_{10}$ is the projection of the spin onto the momentum transfer, while $\hat{\mathcal{O}}_7$ projects the spin perpendicular to that direction [75]. Scattering in the Sun for these operators is thus dominated by elements with unpaired nucleons, namely hydrogen, and (specifically for $\hat{\mathcal{O}}_{10}$ at high m_{χ}) ^{14}Ne . $\hat{\mathcal{O}}_7$ scales as $(\hat{\mathbf{v}}^\perp)^2$, so it benefits from the higher DM velocities within the Sun's gravitational well. This leads to neutrino telescopes being more sensitive in the case of annihilation to W^+W^- and $\tau^+\tau^-$ in the high-mass IceCube

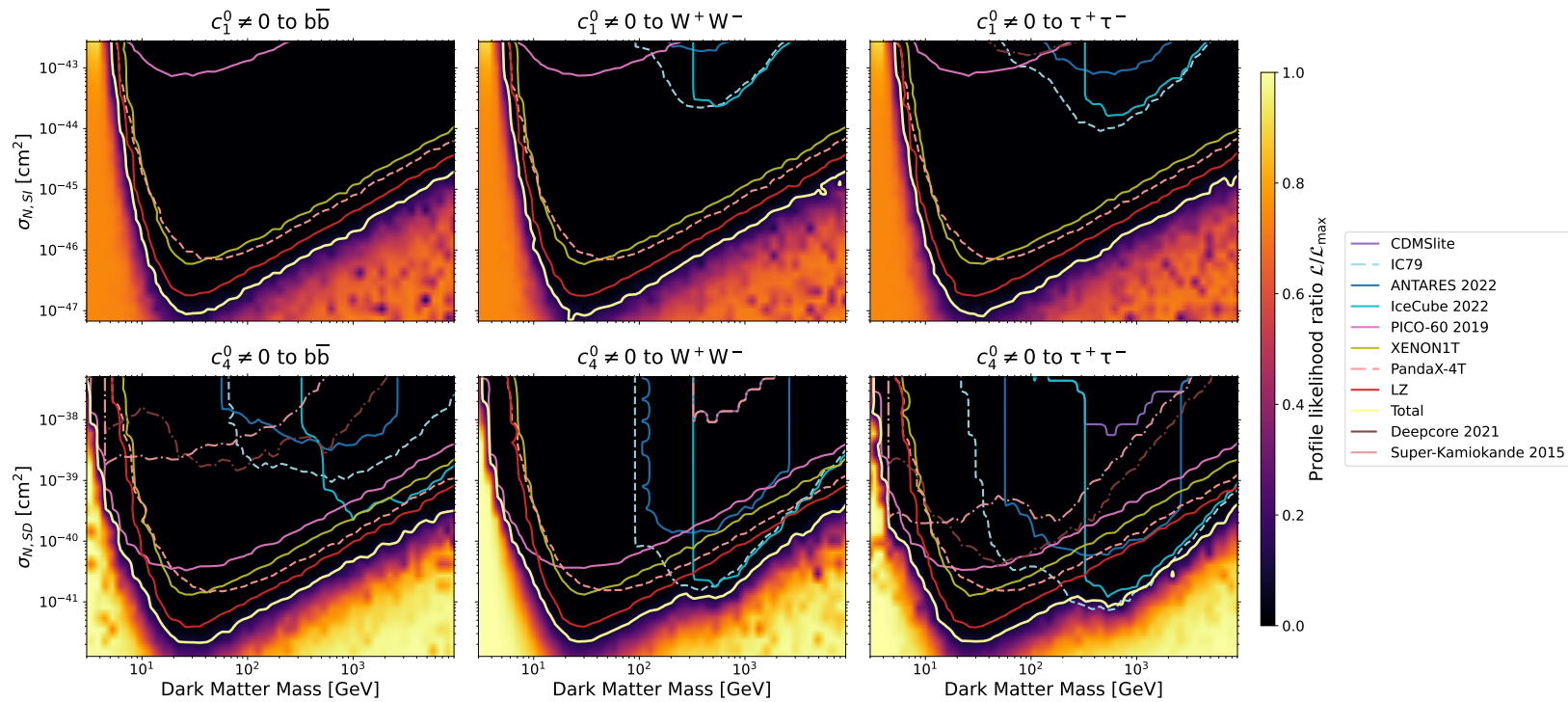


FIG. 1. Profile likelihood ratios in the plane of dark matter mass and effective cross section for c_1^0 (top) and c_4^0 (bottom). These respectively correspond to constant SI and SD cross sections (Eq. 8). Left: annihilation channel to $b\bar{b}$, center: W^+W^- , and right: $\tau^+\tau^-$. The lines indicate the 90% CL contours of the total and each experiment’s contribution to the total. The coloured histogram represents the profile likelihood ratio $\mathcal{L}/\mathcal{L}_{\max}$ of the total. We chose to only display a selection of experiments here that contribute most to the total to reduce visual noise, with complete plots shown in Appendix A. The IC79 line *does not* contribute to the total above 300 GeV as it has overlap with IceCube (2022). The contribution of solar neutrinos becomes more dominant when DD experiments don’t receive the A^2 enhancement and a harder annihilation channel is chosen. These effects manifest in the central and right-hand SD plots as the blue IceCube [13–15, 17] curves dropping below the red LZ [31] curve in the 500 GeV to 1 TeV region.

region, as well as at the lowest masses considered for all annihilation channels, thanks to Super-Kamiokande.

At high masses, the q^2 momentum-dependence of $\hat{\mathcal{O}}_{10}$ leads to a suppression in the Sun, since the large ratio between DM and target mass leads to a low average momentum transfer. Solar capture remains competitive despite this, thanks to the insensitivity of large DD experiments to spin-dependent couplings.

In contrast $\hat{\mathcal{O}}_{11}$ acts as a SI-like interaction but with a q^2 scaling in contrast with the constant scaling of $\hat{\mathcal{O}}_1$. As with $\hat{\mathcal{O}}_{10}$, this leads to a kinematic mismatch between DM and target nuclei in the Sun, in the ~ 100 GeV range where solar constraints dominate. This remains true even despite the fact that $\hat{\mathcal{O}}_{11}$ dominantly scatters with iron (see e.g. Fig. 6 of [20]).

Next, we turn to projections for the sensitivity of future DD and neutrino experiments. We focus on $m_{\text{dm}} = 500$ GeV, where IceCube (2022)’s data are the most constraining, and the W^+W^- final state. A selection of 90% exclusions from DD experiments and neutrino telescopes is shown in the left panel of Fig. 4 for the spin-dependent equivalent coupling c_4^7 . In addition to current experiments, we use GAMBIT to produce future

projections for DARWIN [44] and PICO-500 [45], which we place at 2033 [76] and 2025 [77] respectively. These sensitivities are implemented in DDCalc. These projections have received more recent updates since the previous DDCalc release, but we include them as they still remain relevant to represent the sensitivity of future DD experiments. For DARWIN, DDCalc assumes 200 ton-years of exposure [44], while PICO-500, DDCalc uses the PICO-500 projection assumptions detailed in from [45], namely 250 L fiducial volume of C_3F_8 with 6 live months at 3.2 keV threshold, and 12 months at 10 keV.

In Fig. 4 we also provide an estimate of a future combined neutrino telescope sensitivity, where we assume that sensitivity simply scales with statistics. We estimate the total volume to be twenty times the current IceCube volume, the approximate combined volume of upcoming large-scale optical neutrino telescopes IceCube-Gen2 [78], KM3NeT [79], the Baikal-GVD [80], P-ONE [81], and TRIDENT [82]. The neutrino telescope projection is taken from a reference value for the current exclusion provided by IceCube 2022, and scaling it with the square

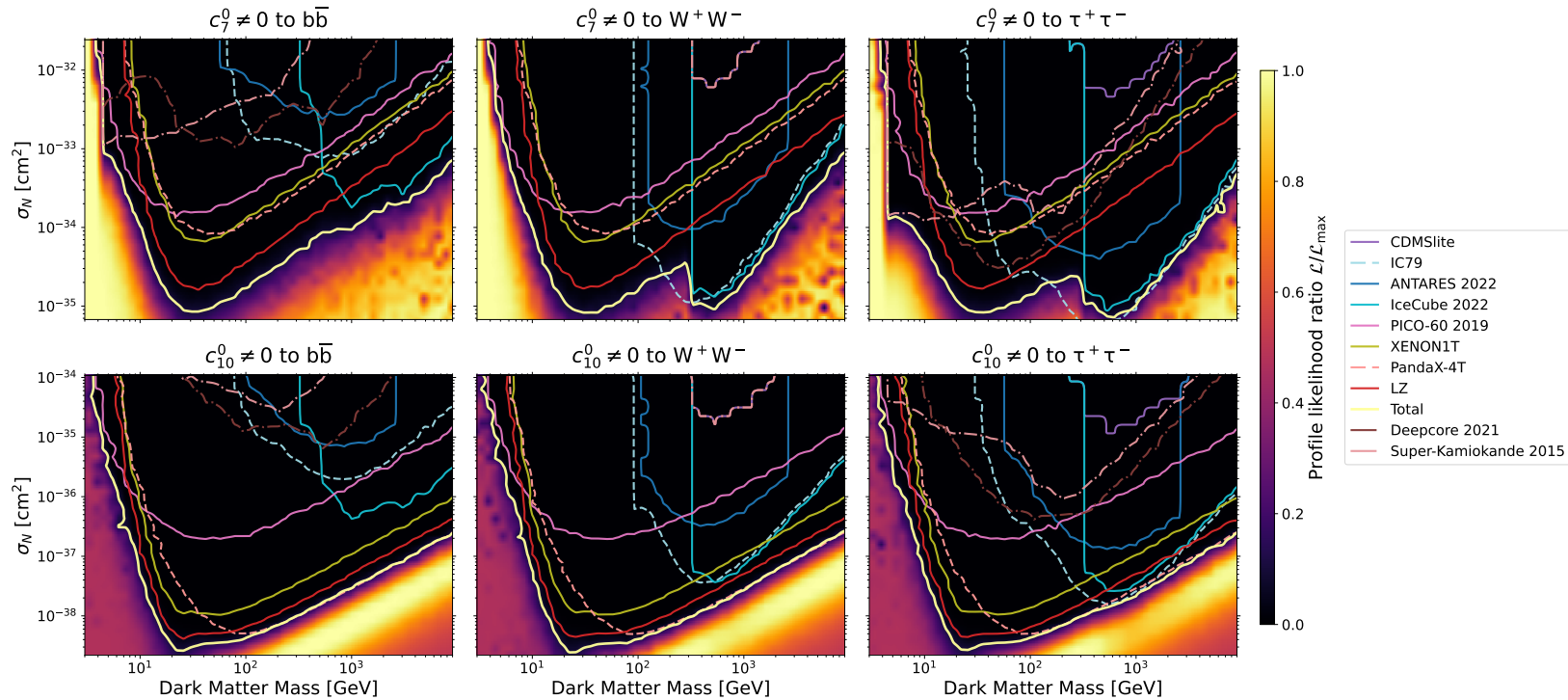


FIG. 2. Same as Fig. 1, but for c_7^0 and c_{10}^0 . The slightly better fit just below the exclusion line in the bottom panel is likely due to an underfluctuation in the LZ event rate at low recoil energies; see main text for details.

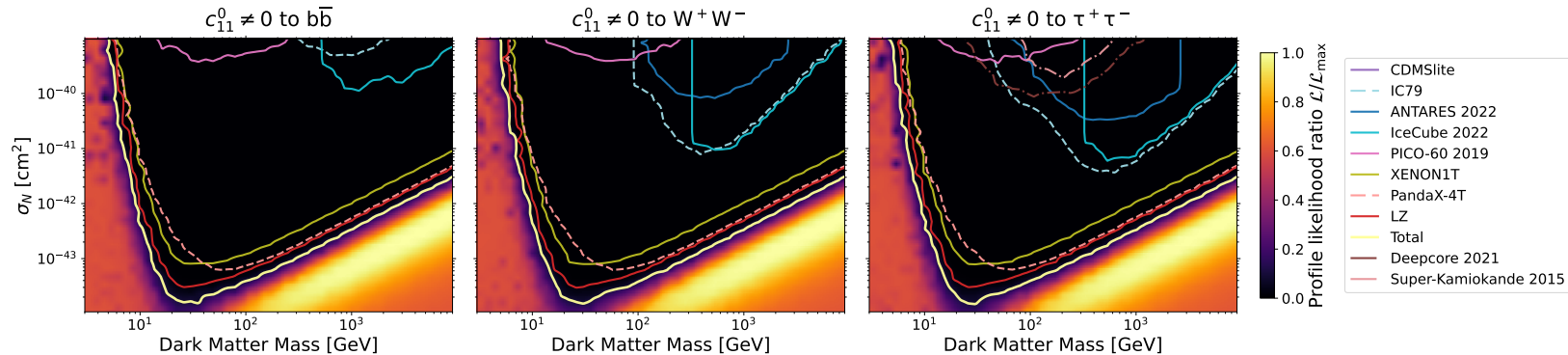


FIG. 3. Same as Fig. 1, but for c_{11}^0 .

root of the scaled volume and duration of experiment:

$$\text{Projection} = \text{IC2022} \left(\frac{V}{V_{\text{IC2022}}} \frac{T}{T_{\text{IC2022}}} \right)^{-\frac{1}{2}}. \quad (17)$$

The left panel of Fig. 4 shows that the excluding power on NREO DM from future underground DD experiments is very likely to outpace that from neutrino telescopes. Only in a tight DM mass window for c_7^τ , as seen in right panel of Fig. 4 does a future projection from neutrino telescopes appear competitive. We show the remaining excluding power plots for each of the 14 operators in Appendix B. Future solar neutrino analyses only outperform future DD experiments for c_7^0 (and perhaps remaining

competitive in the case of c_{14}^0 , see Fig. 26) in a small mass region around $m_{\text{DM}} = 500$ GeV.

VI. CONCLUSIONS

We have presented a global fit of NREO interactions between dark matter and SM particles, combining DD experiments and neutrino telescope observations, including the most recent constraints from IceCube and ANTARES. While these methods remain complementary for some operators, in future DD experiments will remain dominant in most scenarios.

The region of parameter space in which DM annihilation

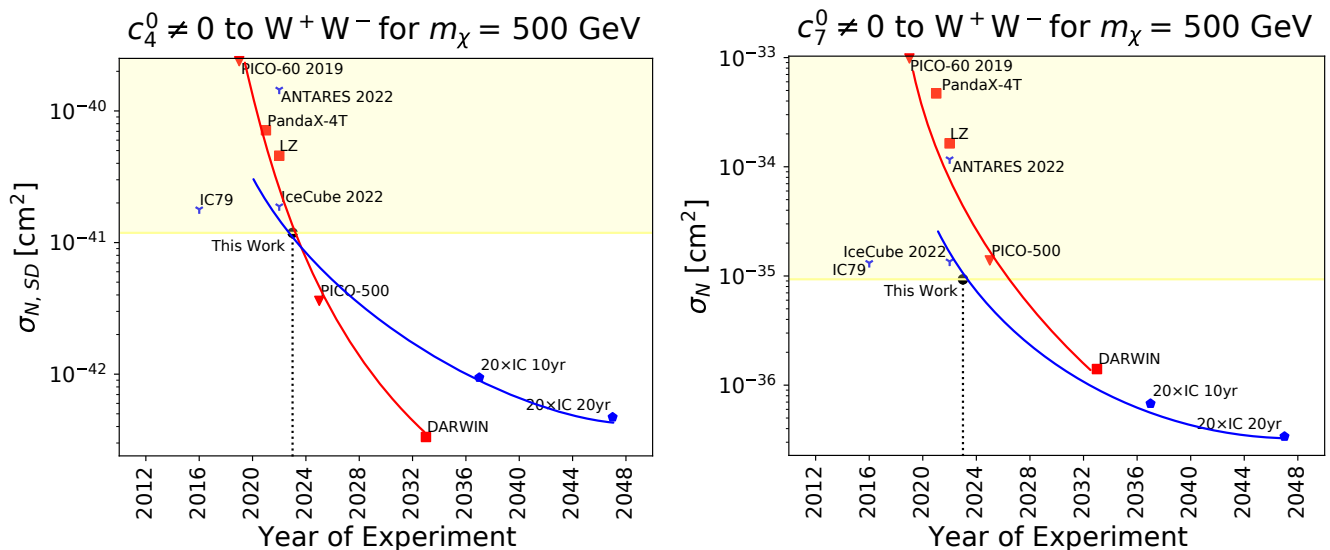


FIG. 4. Here we plot the 90% CL from each experiment at a fixed DM mass of $m_{\text{dm}} = 500 \text{ GeV}$, as a function of year of the experiment. Included are projections from DARWIN [44] and PICO-500 [45] from GAMBIT, and a projection of a future IceCube experiment at twenty times the volume of the current detector. The red (DD) and blue (solar neutrino) lines are drawn to guide the eye. The vertical dotted line indicates the current year and coincides with the point that indicates the current total 90% CL labeled *This Work*. The horizontal light yellow line and region indicates the 90% CL from the total. Left: c_4^0 . Right: c_7^0 . In comparing the left-hand and right-hand plots, we can see that even for couplings like c_4^0 where the current solar neutrino experiments beat current DD experiments, the projections indicate that in future this will not hold. In contrast, for a coupling such as c_7^0 projections indicate that there is a small window of opportunity for future neutrino experiments to continue to be competitive with future DD experiments. The remaining operator couplings can be seen in Appendix B.

lation to neutrino final products exceed sensitivities of constructed DD experiments is thus swiftly closing. The neutrino fog [83–86], which we have not modeled in our projections will become an important background over the next decade, potentially slowing the direct detection side of the race. Simultaneously, solar atmospheric neutrinos (the “neutrino mist”) [87, 88] will begin to pose a challenge to searches for new physics in high-energy neutrinos from the Sun. Both methods thus may well remain competitive and complementary, and, as we have shown, combining the two in a self-consistent and systematic way yields more than the sum of their parts.

ACKNOWLEDGMENTS

We thank Ben Farmer, Felix Kahlhoefer and Sebastian Wild for valuable input. ACV and NPAK are supported by the Arthur B. McDonald Canadian Astroparticle Physics Research Institute, NSERC and the Ontario Ministry of Colleges and Universities, with equipment funded by the Canada Foundation for Innovation and the Ontario Government. Research at Perimeter Institute is supported by the Government of Canada through the Department of Innovation, Science, and Economic Development, and by the Province of Ontario. PS is supported by Australian Research Council Discovery Project DP220100643.

-
- [1] M. Persic, P. Salucci, and F. Stel, *The universal rotation curve of spiral galaxies — I. The dark matter connection*, *Monthly Notices of the Royal Astronomical Society* **281** (1996) 27, [[astro-ph/9506004](#)].
- [2] Planck: N. Aghanim, Y. Akrami, *et. al.*, *Planck 2018 results: VI. Cosmological parameters*, *Astronomy and Astrophysics* **641** (2020) A6, [[arXiv:1807.06209](#)].
- [3] D. G. Cerdeño and A. M. Green, *Direct detection of WIMPs*, in *Particle Dark Matter: Observations, Models and Searches*, pp. 347–369. Cambridge University Press, Cambridge, 2010. [[arXiv:1002.1912](#)].
- [4] M. Lisanti, *Lectures on Dark Matter Physics*, in *New Frontiers in Fields and Strings*, pp. 399–446. WORLD SCIENTIFIC, 2017. [[arXiv:1603.03797](#)].
- [5] M. Schumann, *Direct detection of WIMP dark matter: Concepts and status*, *Journal of Physics G: Nuclear and Particle Physics* **46** (2019) 103003, [[arXiv:1903.03026](#)].
- [6] J. Fan, M. Reece, and L. T. Wang, *Non-relativistic effective theory of dark matter direct detection*, *Journal of Cosmology and Astroparticle Physics* **11** (2010) 042, [[arXiv:1008.1591](#)].

- [7] J. Kumar and D. Marfatia, *Matrix element analyses of dark matter scattering and annihilation*, *Physical Review D* **88** (2013) 014035, [[arXiv:1305.1611](#)].
- [8] A. L. Fitzpatrick, W. Haxton, E. Katz, N. Lubbers, and Y. Xu, *The effective field theory of dark matter direct detection*, *Journal of Cosmology and Astroparticle Physics* **02** (2013) 004, [[arXiv:1203.3542](#)].
- [9] J. B. Dent, L. M. Krauss, J. L. Newstead, and S. Sabharwal, *General analysis of direct dark matter detection: From microphysics to observational signatures*, *Physical Review D* **92** (2015) 063515, [[arXiv:1505.03117](#)].
- [10] Super-Kamiokande: K. Choi, K. Abe, *et al.*, *Search for neutrinos from annihilation of captured low-mass dark matter particles in the Sun by Super-Kamiokande*, *Physical Review Letters* **114** (2015) 141301, [[arXiv:1503.04858](#)].
- [11] ANTARES: S. Adrián-Martínez, A. Albert, *et al.*, *Limits on dark matter annihilation in the sun using the ANTARES neutrino telescope*, *Physics Letters B* **759** (2016) 69–74, [[arXiv:1603.02228](#)].
- [12] ANTARES: C. Poirè, *Indirect Dark Matter search towards the Sun with the ANTARES neutrino telescope*, *Journal of Physics: Conference Series* **2156** (2021) 012039.
- [13] IceCube: M. G. Aartsen, R. Abbasi, *et al.*, *Search for dark matter annihilations in the sun with the 79-string icecube detector*, *Physical Review Letters* **110** (2013) 131302, [[arXiv:1212.4097](#)].
- [14] IceCube: P. Scott, C. Savage, *et al.*, *Use of event-level neutrino telescope data in global fits for theories of new physics*, *Journal of Cosmology and Astroparticle Physics* **11** (2012) 057, [[arXiv:1207.0810](#)].
- [15] IceCube: M. G. Aartsen, K. Abraham, *et al.*, *Improved limits on dark matter annihilation in the Sun with the 79-string IceCube detector and implications for supersymmetry*, *Journal of Cosmology and Astroparticle Physics* **04** (2016) 022, [[arXiv:1601.00653](#)].
- [16] IceCube: C. A. Argüelles, A. Kheirandish, J. Lazar, and Q. Liu, *Search for Dark Matter Annihilation to Neutrinos from the Sun*, *Proceedings of Science ICRC2019* (2021) 527, [[arXiv:1909.03930](#)].
- [17] IceCube: R. Abbasi, M. Ackermann, *et al.*, *Searching for Dark Matter from the Sun with the IceCube Detector*, in *Proceedings of Science*, (Berlin, Germany - Online), Sissa Medialab **ICRC2021** (2022) 020.
- [18] A. C. Vincent, A. Serenelli, and P. Scott, *Generalised form factor dark matter in the Sun*, *Journal of Cosmology and Astroparticle Physics* **08** (2015) 040, [[arXiv:1504.04378](#)].
- [19] R. Catena and B. Schwabe, *Form factors for dark matter capture by the Sun in effective theories*, *Journal of Cosmology and Astroparticle Physics* **04** (2015) 042, [[arXiv:1501.03729](#)].
- [20] R. Catena, *Dark matter signals at neutrino telescopes in effective theories*, *Journal of Cosmology and Astroparticle Physics* **04** (2015) 052, [[arXiv:1503.04109](#)].
- [21] R. Catena and F. Hellström, *New constraints on inelastic dark matter from IceCube*, *Journal of Cosmology and Astroparticle Physics* **10** (2018) 039, [[arXiv:1808.08082](#)].
- [22] A. Brenner, G. Herrera, *et al.*, *Complementarity of experiments in probing the non-relativistic effective theory of dark matter-nucleon interactions*, *Journal of Cosmology and Astroparticle Physics* **06** (2022) 026, [[arXiv:2203.04210](#)].
- [23] GAMBIT: P. Athron, C. Balazs, *et al.*, *GAMBIT: The global and modular beyond-the-standard-model inference tool*, *European Physical Journal C* **77** (2018) 784, [[arXiv:1705.07908](#)].
- [24] S. S. AbdusSalam, F. J. Agocs, *et al.*, *Simple and statistically sound recommendations for analysing physical theories*, *Reports on Progress in Physics* **85** (2022) 052201, [[arXiv:2012.09874](#)].
- [25] SuperCDMS: R. Agnese, A. J. Anderson, *et al.*, *New Results from the Search for Low-Mass Weakly Interacting Massive Particles with the CDMS Low Ionization Threshold Experiment*, *Physical Review Letters* **116** (2016) 071301, [[arXiv:1509.02448](#)].
- [26] CRESST: G. Angloher, A. Bento, *et al.*, *Results on light dark matter particles with a low-threshold CRESST-II detector*, *European Physical Journal C* **76** (2016) 25, [[arXiv:1509.01515](#)].
- [27] CRESST: A. H. Abdelhameed, G. Angloher, *et al.*, *First results from the CRESST-III low-mass dark matter program*, *Physical Review D* **100** (2019) 102002, [[arXiv:1904.00498](#)].
- [28] DarkSide: P. Agnes, I. F. Albuquerque, *et al.*, *DarkSide-50 532-day dark matter search with low-radioactivity argon*, *Physical Review D* **98** (2018) 102006, [[arXiv:1802.07198](#)].
- [29] DarkSide: P. Agnes, I. F. M. Albuquerque, *et al.*, *Low-Mass Dark Matter Search with the DarkSide-50 Experiment*, *Physical Review Letters* **121** (2018) 081307, [[arXiv:1802.06994](#)].
- [30] LUX: D. S. Akerib, S. Alsum, *et al.*, *Results from a Search for Dark Matter in the Complete LUX Exposure*, *Physical Review Letters* **118** (2017) 021303, [[arXiv:1608.07648](#)].
- [31] LZ: J. Aalbers, D. S. Akerib, *et al.*, *First Dark Matter Search Results from the LUX-ZEPLIN (LZ) Experiment*, *Physical Review Letters* **131** (2023) 041002, [[arXiv:2207.03764](#)].
- [32] PandaX-II: A. Tan, M. Xiao, *et al.*, *Dark Matter Results from First 98.7 Days of Data from the PandaX-II Experiment*, *Physical Review Letters* **117** (2016) 121303, [[arXiv:1607.07400](#)].
- [33] PandaX-II: X. Cui, A. Abdurkerim, *et al.*, *Dark Matter Results from 54-Ton-Day Exposure of PandaX-II Experiment*, *Physical Review Letters* **119** (2017) 181302, [[arXiv:1708.06917](#)].
- [34] PandaX-4T: Y. Meng, Z. Wang, *et al.*, *Dark Matter Search Results from the PandaX-4T Commissioning Run*, *Physical Review Letters* **127** (2021) 261802, [[arXiv:2107.13438](#)].
- [35] PICO: C. Amole, M. Ardid, *et al.*, *Improved dark matter search results from PICO-2L Run 2*, *Physical Review D* **93** (2016) 061101, [[arXiv:1601.03729](#)].
- [36] PICO: C. Amole, M. Ardid, *et al.*, *Dark Matter Search Results from the PICO-60 CFS.35I Bubble Chamber*, *Physical Review D* **93** (2016) 052014, [[arXiv:1510.07754](#)].
- [37] PICO: C. Amole, M. Ardid, *et al.*, *Dark Matter Search Results from the PICO-60 C3 F8 Bubble Chamber*, *Physical Review Letters* **118** (2017) 251301, [[arXiv:1702.07666](#)].

- [38] PICO: C. Amole, M. Ardid, *et. al.*, *Dark matter search results from the complete exposure of the PICO-60 C3 F8 bubble chamber*, *Physical Review D* **100** (2019) 022001, [[arXiv:1902.04031](#)].
- [39] SIMPLE: M. Felizardo, T. A. Girard, *et. al.*, *The SIMPLE Phase II Dark Matter Search*, *Physical Review D* **89** (2014) 072013, [[arXiv:1404.4309](#)].
- [40] XENON100: E. Aprile, M. Alfonsi, *et. al.*, *Dark Matter Results from 225 Live Days of XENON100 Data*, *Physical Review Letters* **109** (2012) 181301, [[arXiv:1207.5988](#)].
- [41] XENON: E. Aprile, J. Aalbers, *et. al.*, *Dark Matter Search Results from a One Ton-Year Exposure of XENON1T*, *Physical Review Letters* **121** (2018) 111302, [[arXiv:1805.12562](#)].
- [42] C. Poirè, *Limits for Dark Matter annihilation in the Sun with ANTARES neutrino telescope*, 2022, <https://indi.to/Pp2XC>.
- [43] IceCube: R. Abbasi, M. Ackermann, *et. al.*, *Search for GeV-scale Dark Matter Annihilation in the Sun with IceCube DeepCore*, *Physical Review D* **105** (2022) 062004, [[arXiv:2111.09970](#)].
- [44] M. Schumann, L. Baudis, L. Büttikofer, A. Kish, and M. Selvi, *Dark matter sensitivity of multi-ton liquid xenon detectors*, *Journal of Cosmology and Astroparticle Physics* **10** (2015) 016, [[arXiv:1506.08309](#)].
- [45] S. Fallows, *Toward a next-generation dark matter search with the PICO-40L bubble chamber*, 2017, <https://indi.to/zYZVC>.
- [46] GAMBIT: P. Athron, N. Avis Kozar, *et. al.*, *Thermal WIMPs and the scale of new physics: Global fits of Dirac dark matter effective field theories*, *European Physical Journal C* **81** (2021) 992, [[arXiv:2106.02056](#)].
- [47] N. P. Avis Kozar, P. Scott, and A. C. Vincent, *Supplementary Data: A global fit of non-relativistic effective dark matter operators including solar neutrinos*, 2023, <https://zenodo.org/records/10032218>.
- [48] N. Anand, A. L. Fitzpatrick, and W. C. Haxton, *Weakly interacting massive particle-nucleus elastic scattering response*, *Physical Review C - Nuclear Physics* **89** (2014) 065501, [[arXiv:1308.6288](#)].
- [49] M. T. Frandsen, F. Kahlhoefer, C. McCabe, S. Sarkar, and K. Schmidt-Hoberg, *Resolving astrophysical uncertainties in dark matter direct detection*, *Journal of Cosmology and Astroparticle Physics* **01** (2012) 024, [[arXiv:1111.0292](#)].
- [50] DEAP: P. Adhikari, R. Ajaj, *et. al.*, *Constraints on dark matter-nucleon effective couplings in the presence of kinematically distinct halo substructures using the DEAP-3600 detector*, *Physical Review D* **102** (2020) 082001, [[arXiv:2005.14667](#)].
- [51] Particle Data Group: R. L. Workman, V. D. Burkert, *et. al.*, *Review of Particle Physics*, *Progress of Theoretical and Experimental Physics* **2022** (2022) 083C01.
- [52] P. Scott, M. Fairbairn, and J. Edsjö, *Dark stars at the Galactic Centre - The main sequence*, *Monthly Notices of the Royal Astronomical Society* **394** (2009) 82, [[arXiv:0809.1871](#)].
- [53] A. Gould, *Resonant enhancements in weakly interacting massive particle capture by the earth*, *The Astrophysical Journal* **321** (1987) 571.
- [54] G. Busoni, A. D. Simone, P. Scott, and A. C. Vincent, *Evaporation and scattering of momentum- and velocity-dependent dark matter in the Sun*, *Journal of Cosmology and Astroparticle Physics* **10** (2017) 037, [[arXiv:1703.07784](#)].
- [55] Super-Kamiokande: Y. Fukuda, T. Hayakawa, *et. al.*, *Measurements of the solar neutrino flux from super-kamiokande's first 300 days*, *Physical Review Letters* **81** (1998) 1158–1162, [[hep-ex/9805021](#)].
- [56] P. Gondolo, J. Edsjö, *et. al.*, *DarkSUSY: Computing supersymmetric dark matter properties numerically*, *Journal of Cosmology and Astroparticle Physics* **07** (2004) 008, [[astro-ph/0406204](#)].
- [57] T. Bringmann, T. Edsjö, P. Gondolo, P. Ullio, and L. Bergström, *DarkSUSY 6 : An Advanced Tool to Compute Dark Matter Properties Numerically*, *Journal of Cosmology and Astroparticle Physics* **07** (2018) 033, [[arXiv:1802.03399](#)].
- [58] GAMBIT Dark Matter Workgroup: T. Bringmann, J. Conrad, *et. al.*, *DarkBit: A GAMBIT module for computing dark matter observables and likelihoods*, *European Physical Journal C* **77** (2017) 831, [[arXiv:1705.07920](#)].
- [59] GAMBIT: P. Athron, C. Balázs, *et. al.*, *Global analyses of Higgs portal singlet dark matter models using GAMBIT*, *European Physical Journal C* **79** (2019) 38, [[arXiv:1808.10465](#)].
- [60] N. Avis Kozar, A. Caddell, L. Fraser-Leach, P. Scott, and A. C. Vincent, *Capt'n General: A generalized stellar dark matter capture and heat transport code*, in *Tools for High Energy Physics and Cosmology*, (Lyon) (2021) [[arXiv:2105.06810](#)].
- [61] GAMBIT Models Workgroup: P. Athron, C. Balázs, *et. al.*, *SpecBit, DecayBit and PrecisionBit: GAMBIT modules for computing mass spectra, particle decay rates and precision observables*, *European Physical Journal C* **78** (2018) 22, [[arXiv:1705.07936](#)].
- [62] GAMBIT: G. D. Martinez, J. McKay, *et. al.*, *Comparison of statistical sampling methods with ScannerBit, the GAMBIT scanning module*, *European Physical Journal C* **77** (2017) 761, [[arXiv:1705.07959](#)].
- [63] A. Putze and L. Derome, *The Grenoble Analysis Toolkit (GreAT)-A statistical analysis framework*, *Physics of the Dark Universe* **5–6** (2014) 29–34.
- [64] F. Feroz, M. P. Hobson, and M. Bridges, *MultiNest: An efficient and robust Bayesian inference tool for cosmology and particle physics*, *Monthly Notices of the Royal Astronomical Society* **398** (2009) 1601–1614, [[arXiv:0809.3437](#)].
- [65] R. Piessens, E. deDoncker-Kapenga, C. Ueberhuber, and D. Kahaner, *QUADPACK: A Subroutine Package for Automatic Integration*, vol. 1 of *Springer Series in Computational Mathematics*. Springer Science & Business Media, Berlin Heidelberg, 1983.
- [66] S. Meighen-Berger, *Dark Matter Searches with IceCube*, 2022, <https://indi.to/n3Sh2>.
- [67] DarkMachines High Dimensional Sampling Group: C. Balázs, M. van Beekveld, *et. al.*, *A comparison of optimisation algorithms for high-dimensional particle and astrophysics applications*, *Journal of High Energy Physics* **05** (2021) 108, [[arXiv:2101.04525](#)].
- [68] D. Hooper and G. D. Kribs, *Probing Kaluza-Klein dark matter with neutrino telescopes*, *Phys. Rev. D* **67** (2003) 055003, [[hep-ph/0208261](#)].

- [69] A. Cheek, D. D. Price, and E. M. Sandford, *Isospin-violating dark matter at liquid noble detectors: New constraints, future projections, and an exploration of target complementarity*, *European Physical Journal C* **83** (2023) 914, [[arXiv:2302.05458](#)].
- [70] M. J. Reid, K. M. Menten, *et. al.*, *Trigonometric Parallaxes of High Mass Star Forming Regions: The Structure and Kinematics of the Milky Way*, *The Astrophysical Journal* **783** (2014) 130, [[arXiv:1401.5377](#)].
- [71] A. J. Deason, A. Fattahi, *et. al.*, *The local high velocity tail and the Galactic escape speed*, *Monthly Notices of the Royal Astronomical Society* **485** (2019) 3514–3526, [[arXiv:1901.02016](#)].
- [72] P. Scott, *Pippi - painless parsing, post-processing and plotting of posterior and likelihood samples*, *The European Physical Journal Plus* **127** (2012) 138, [[arXiv:1206.2245](#)].
- [73] J. D. Hunter, *Matplotlib: A 2D Graphics Environment*, *Computing in Science & Engineering* **9** (2007) 90–95.
- [74] I. Flyamer, Z. Xue, *et. al.*, “Phlya/adjustText: 0.8.” Zenodo, 2023, <https://github.com/Phlya/adjustText>.
- [75] A. L. Fitzpatrick, W. Haxton, E. Katz, N. Lubbers, and Y. Xu, *Model Independent Direct Detection Analyses*, 2012, <http://arxiv.org/abs/1211.2818>.
- [76] J. Cooley, T. Lin, *et. al.*, *Report of the Topical Group on Particle Dark Matter for Snowmass 2021*, [[arXiv:2209.07426](#)].
- [77] D. S. Akerib, P. B. Cushman, *et. al.*, *Snowmass2021 Cosmic Frontier Dark Matter Direct Detection to the Neutrino Fog*, [[arXiv:2203.08084](#)].
- [78] IceCube-Gen2: M. G. Aartsen, R. Abbasi, *et. al.*, *IceCube-Gen2: The Window to the Extreme Universe*, *Journal of Physics G: Nuclear and Particle Physics* **48** (2021) 060501, [[arXiv:2008.04323](#)].
- [79] KM3Net: S. Adrián-Martínez, M. Ageron, *et. al.*, *Letter of intent for KM3NeT 2.0*, *Journal of Physics G: Nuclear and Particle Physics* **43** (2016) 084001, [[arXiv:1601.07459](#)].
- [80] Baikal-GVD: A. D. Avrorin, A. V. Avrorin, *et. al.*, *Baikal-GVD: Status and prospects*, *EPJ Web of Conferences* **191** (2018) 01006, [[arXiv:1808.10353](#)].
- [81] P-ONE: M. Agostini, M. Böhmer, *et. al.*, *The Pacific Ocean Neutrino Experiment*, *Nature Astronomy* **4** (2020) 913–915, [[arXiv:2005.09493](#)].
- [82] Z. P. Ye, F. Hu, *et. al.*, *A multi-cubic-kilometre neutrino telescope in the western Pacific Ocean*, [[arXiv:2207.04519](#)].
- [83] J. Monroe and P. Fisher, *Neutrino Backgrounds to Dark Matter Searches*, *Physical Review D* **76** (2007) 033007, [[arXiv:0706.3019](#)].
- [84] L. E. Strigari, *Neutrino Coherent Scattering Rates at Direct Dark Matter Detectors*, *New Journal of Physics* **11** (2009) 105011, [[arXiv:0903.3630](#)].
- [85] J. Billard, E. Figueroa-Feliciano, and L. Strigari, *Implication of neutrino backgrounds on the reach of next generation dark matter direct detection experiments*, *Physical Review D* **89** (2014) 023524, [[arXiv:1307.5458](#)].
- [86] C. A. J. O’Hare, *New Definition of the Neutrino Floor for Direct Dark Matter Searches*, *Physical Review Letters* **127** (2021) 251802, [[arXiv:2109.03116](#)].
- [87] K. C. Y. Ng, J. F. Beacom, A. H. G. Peter, and C. Rott, *Solar Atmospheric Neutrinos: A New Neutrino Floor for Dark Matter Searches*, *Physical Review D* **96** (2017) 103006, [[arXiv:1703.10280](#)].
- [88] C. A. Argüelles, G. de Wasseige, A. Fedynitch, and B. J. P. Jones, *Solar Atmospheric Neutrinos and the Sensitivity Floor for Solar Dark Matter Annihilation Searches*, *Journal of Cosmology and Astroparticle Physics* **07** (2017) 024, [[arXiv:1703.07798](#)].

Appendix A: All Scans

	CDMSlite		PICO-60 2017		XENON1T
	CRESST-II		PICO-60 2019		PandaX-4T
	CRESST-III		DarkSide-50		LZ
	IC79		DarkSide-50 S2 Only		Total
	ANTARES 2022		XENON100		PICO-500
	IceCube 2022		LUX 2016		DARWIN
	SIMPLE		PandaX-II 2016		Deepcore 2021
	PICO-2L		PandaX-II 2017		Super-Kamiokande 2015
	PICO-60				

FIG. 5. The legend of experiment likelihoods for all plots, rendered separately so that the plots themselves can be viewed more clearly on their own.

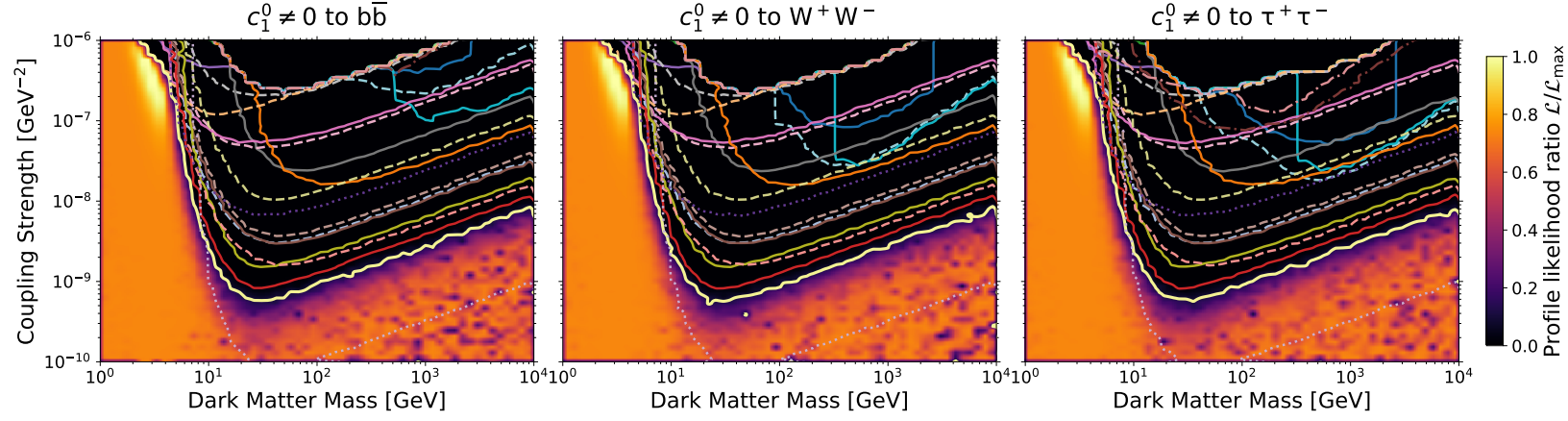


FIG. 6. Profile likelihood ratios in the plane of dark matter mass and coupling strength for c_1^0 . Left: annihilation channel to $b\bar{b}$, center: W^+W^- , and right: $\tau^+\tau^-$. The lines indicate the 90% CL contours of the total and each experiment's contribution to the total. The coloured histogram represents the profile likelihood ratio $\mathcal{L}/\mathcal{L}_{\max}$ of the total. The legend for each experiment's contour can be seen in Fig. 5. The IC79 line *does not* contribute to the total above 300 GeV as it has overlap with IceCube (2022).

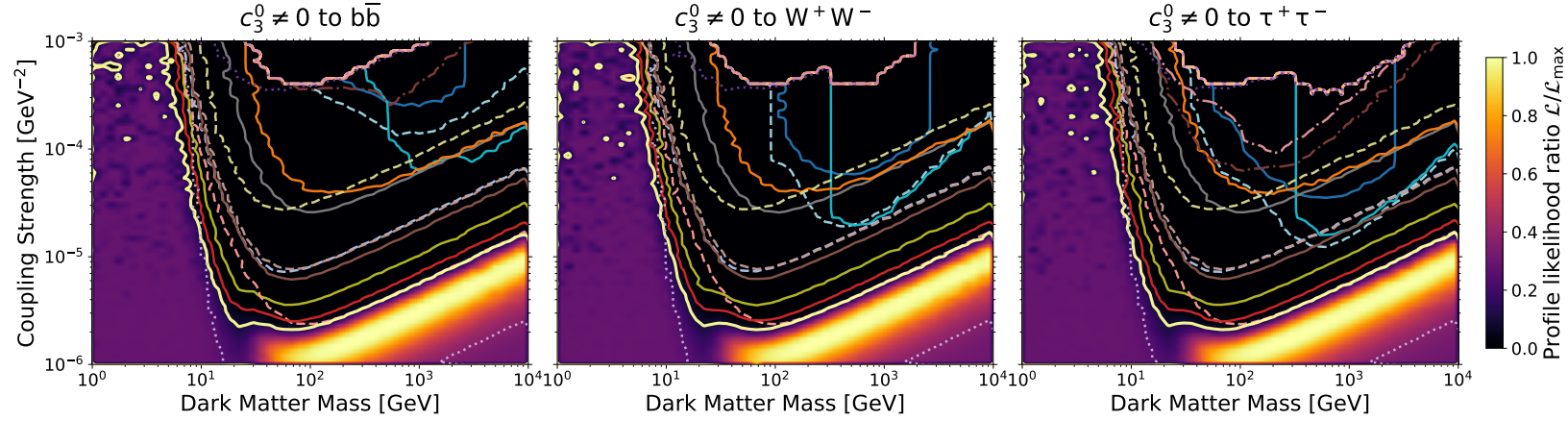


FIG. 7. Same as Fig. 6, but for c_3^0 .

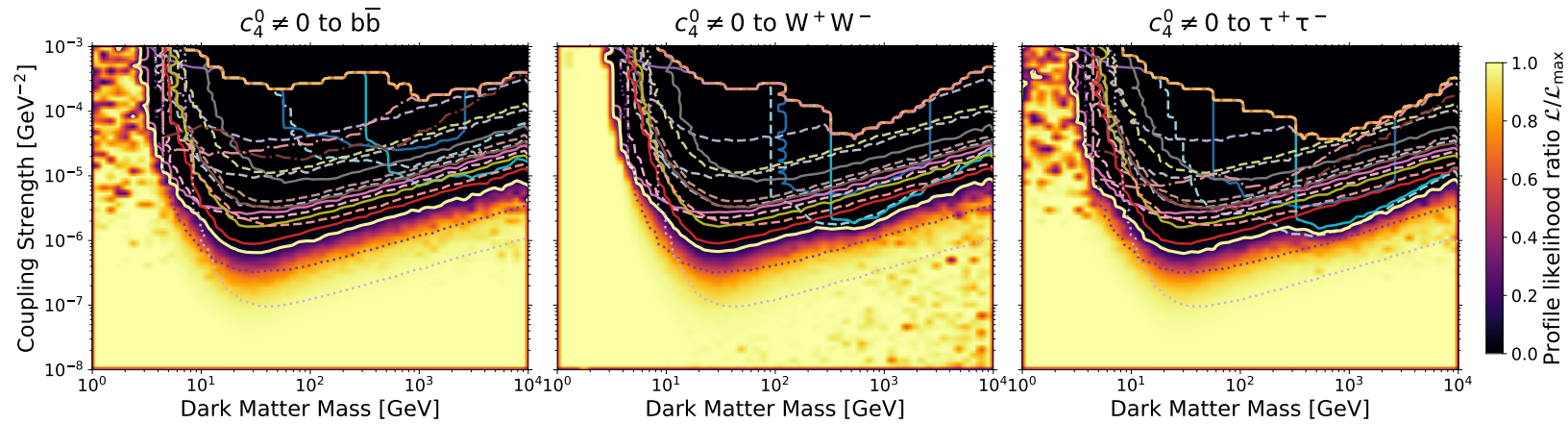
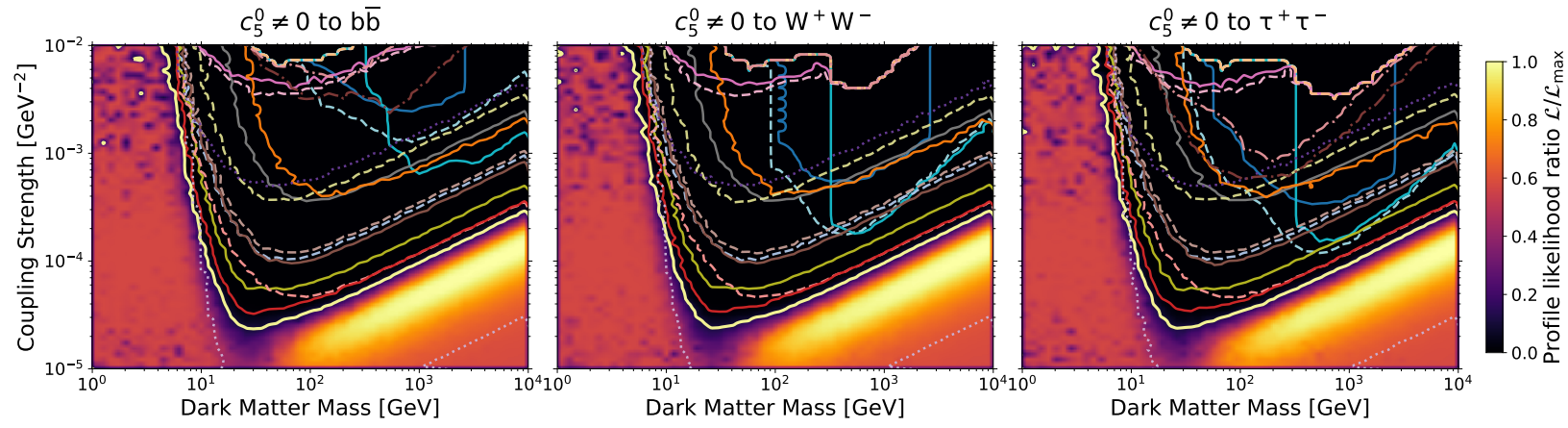
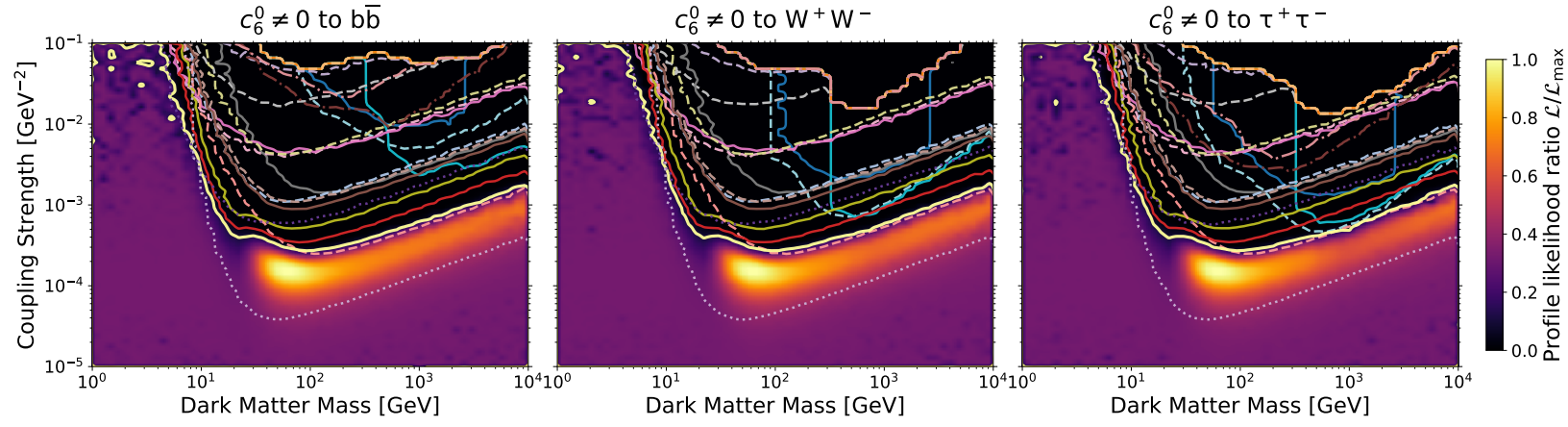
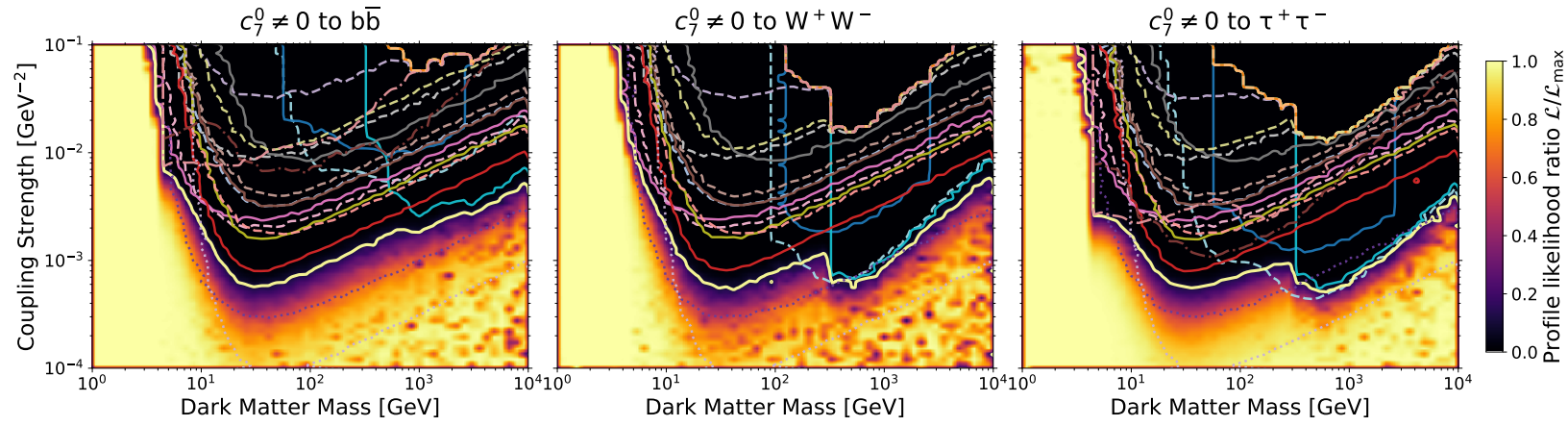
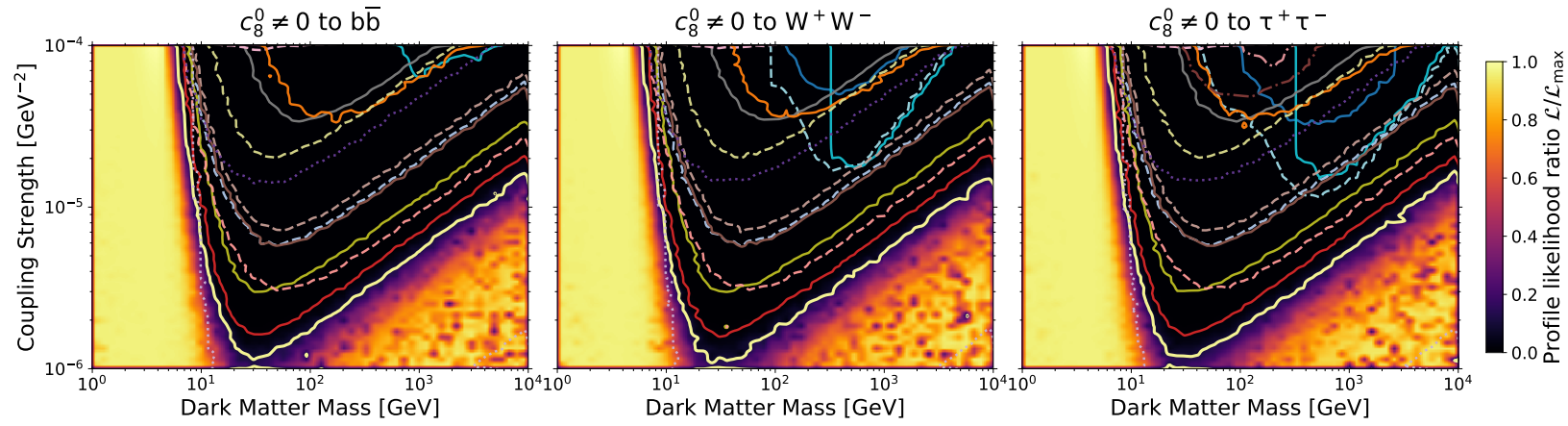
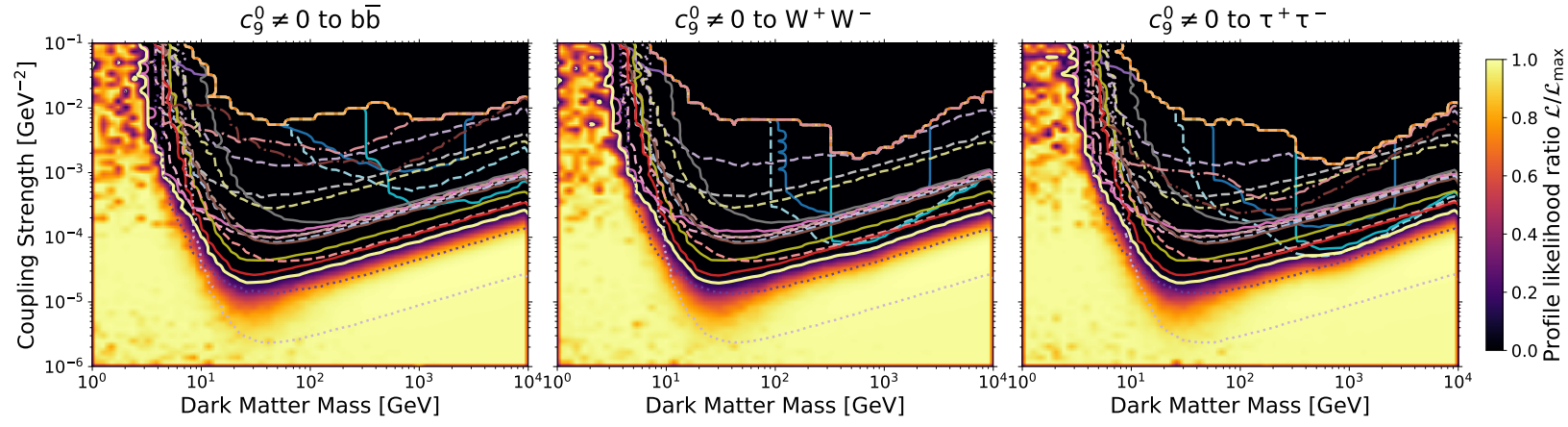
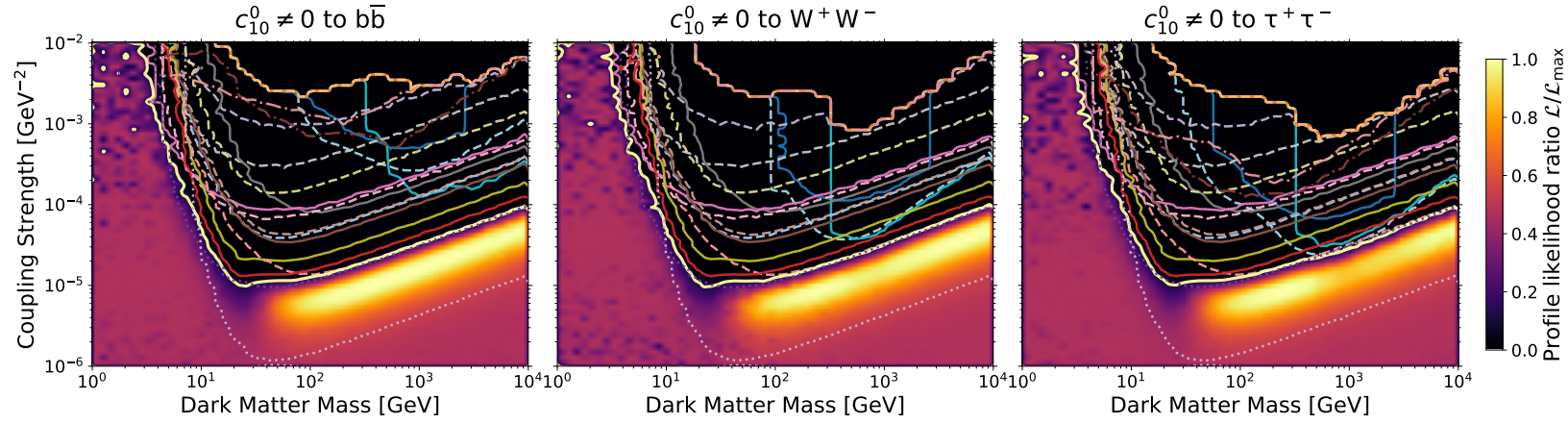
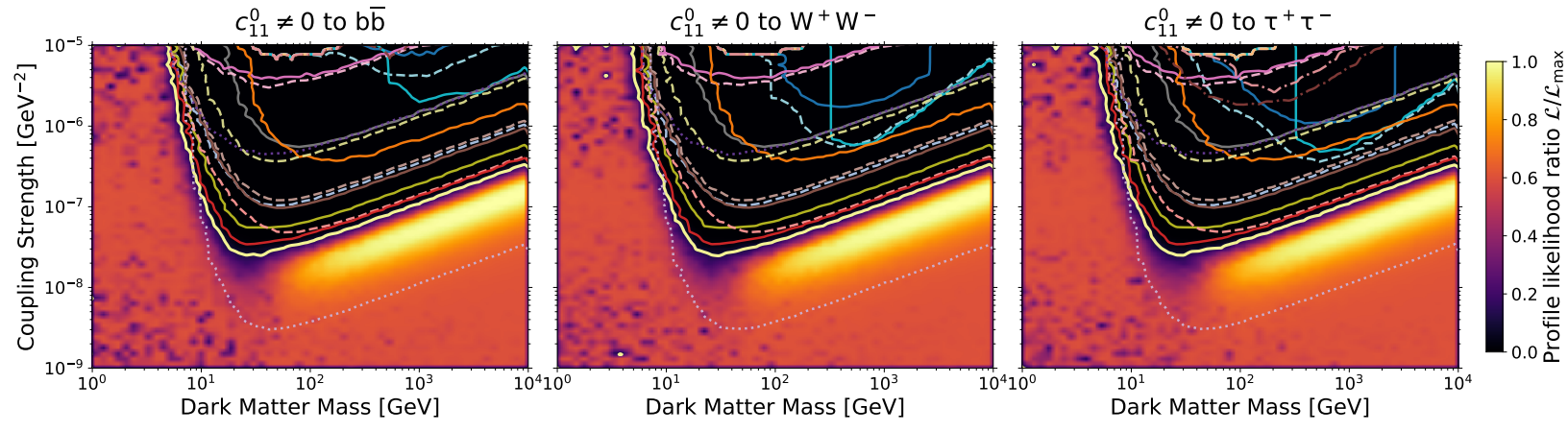
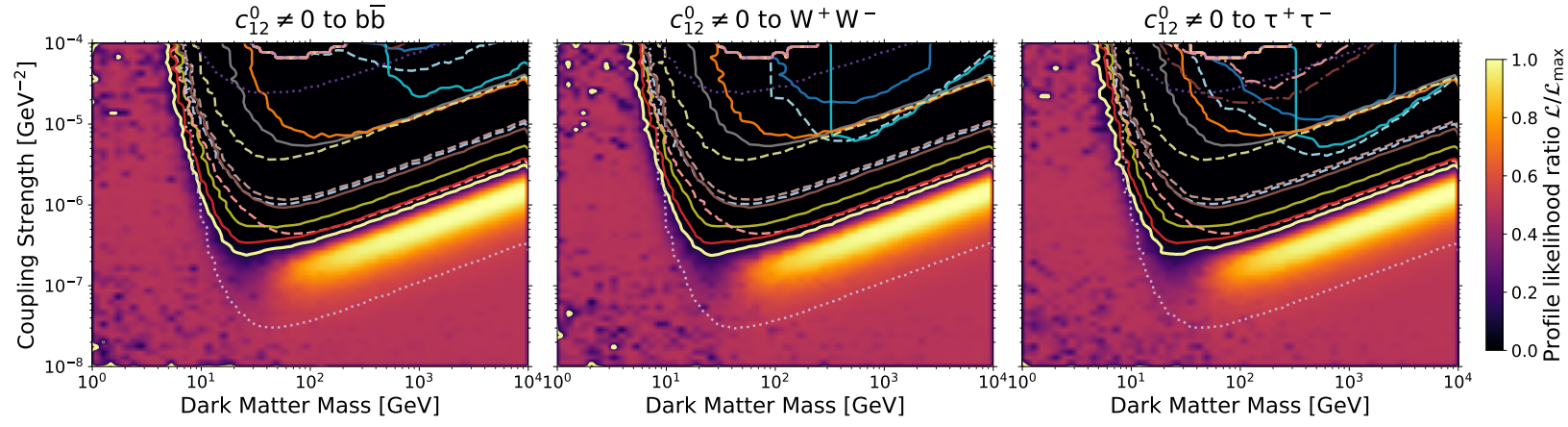
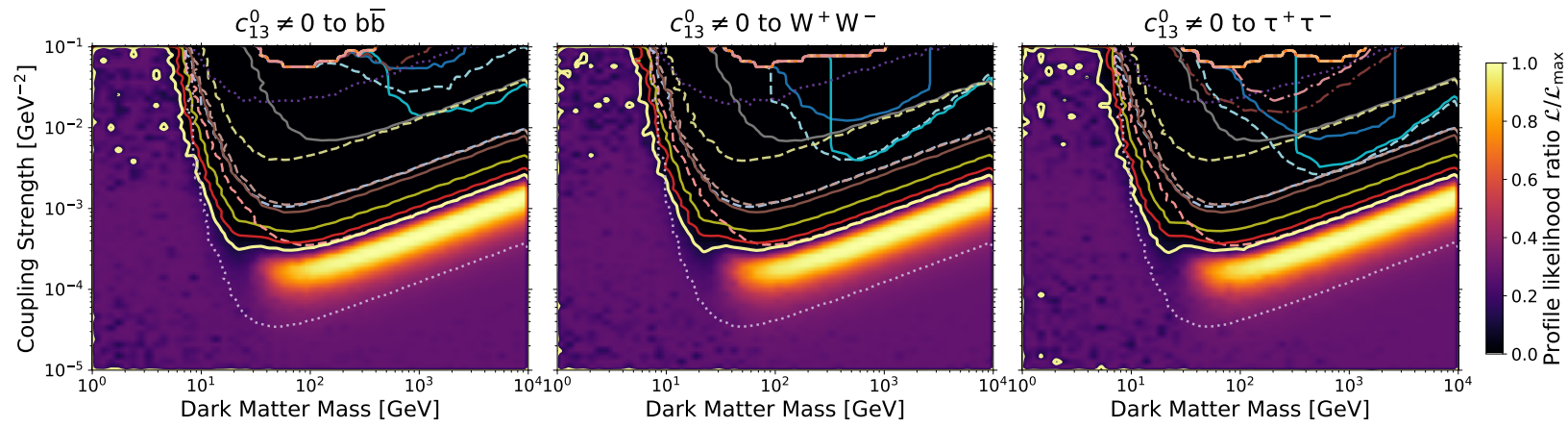
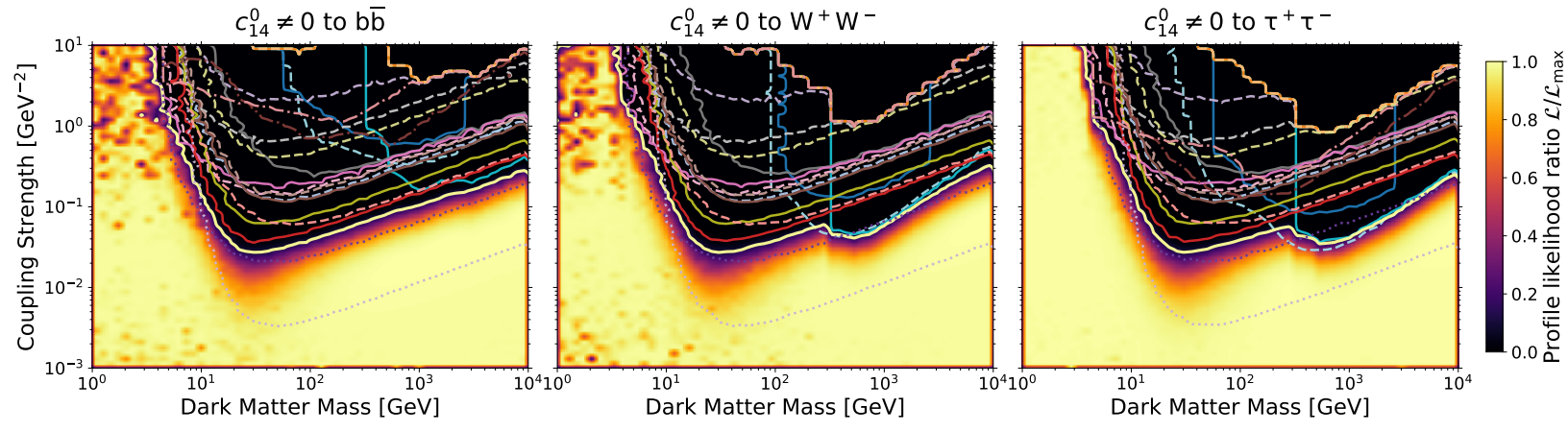
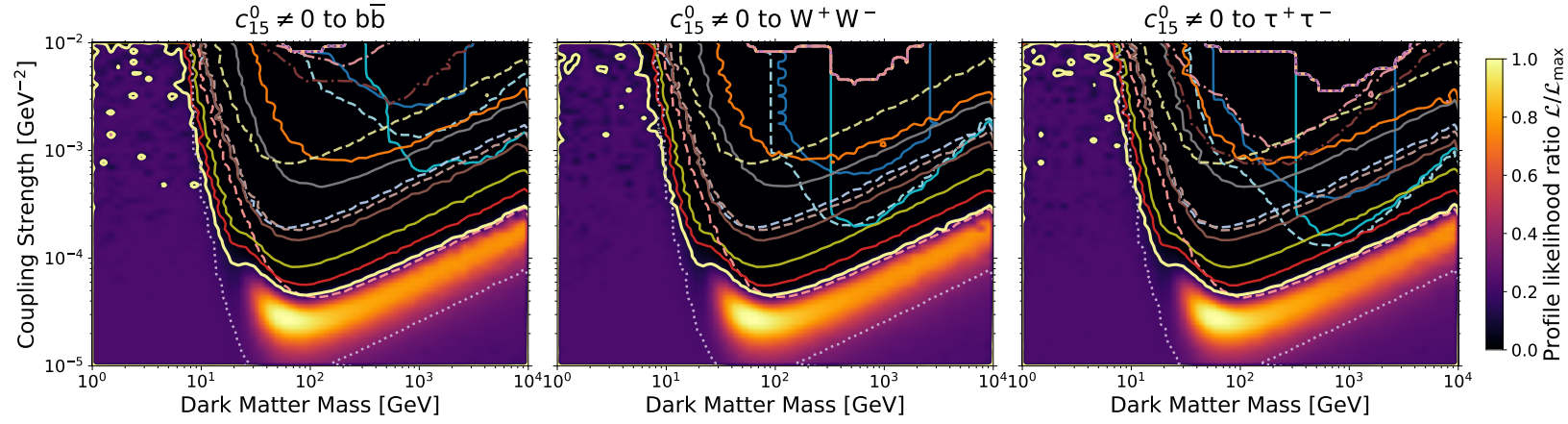


FIG. 8. Same as Fig. 6, but for c_4^0 .

FIG. 9. Same as Fig. 6, but for c_5^0 .FIG. 10. Same as Fig. 6, but for c_6^0 .FIG. 11. Same as Fig. 6, but for c_7^0 .

FIG. 12. Same as Fig. 6, but for c_8^0 .FIG. 13. Same as Fig. 6, but for c_9^0 .FIG. 14. Same as Fig. 6, but for c_{10}^0 .

FIG. 15. Same as Fig. 6, but for c_{11}^0 .FIG. 16. Same as Fig. 6, but for c_{12}^0 .FIG. 17. Same as Fig. 6, but for c_{13}^0 .

FIG. 18. Same as Fig. 6, but for c_{14}^0 .FIG. 19. Same as Fig. 6, but for c_{15}^0 .

Appendix B: Projection Plots

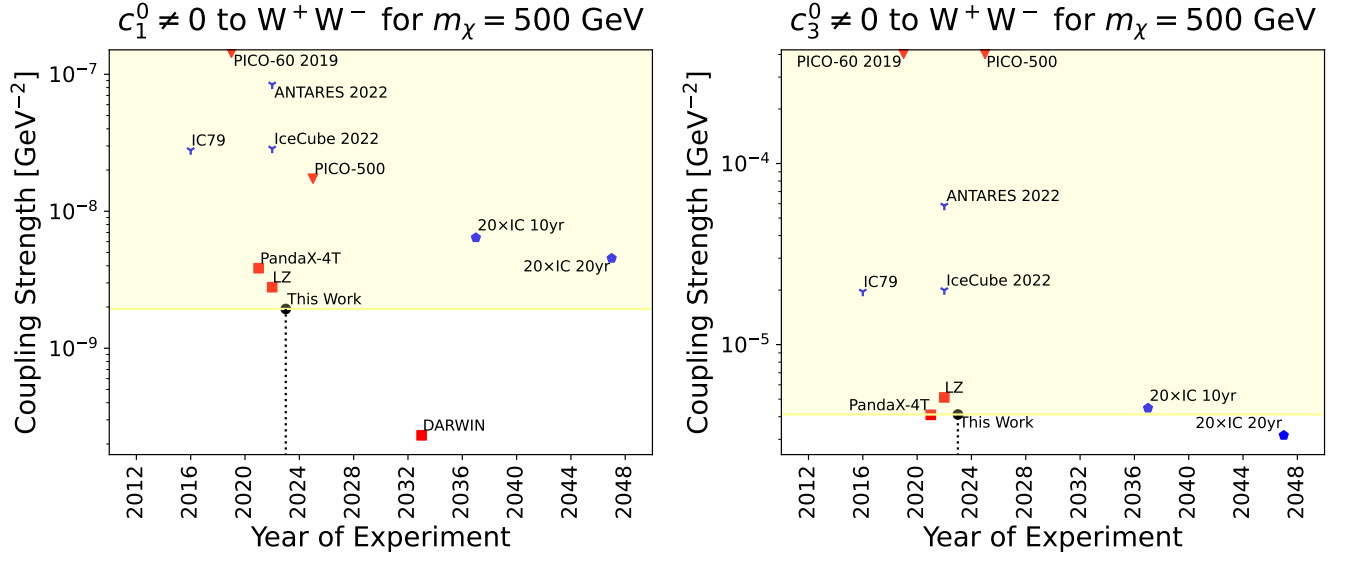


FIG. 20. Here we plot the 90% CL from each experiment at a fixed DM mass of $m_{\text{dm}} = 500$ GeV, as a function of year of the experiment. Included are projections from DARWIN [44] and PICO-500 [45] from GAMBIT, and a projection of a future IceCube experiment at twenty times the volume of the current detector. The vertical black dotted line indicates the current year and coincides with the point that indicates the current total 90% CL labeled *This Work*. The horizontal light yellow line and region indicates the 90% CL from the total. Left: c_1^0 . Right: c_3^0 .

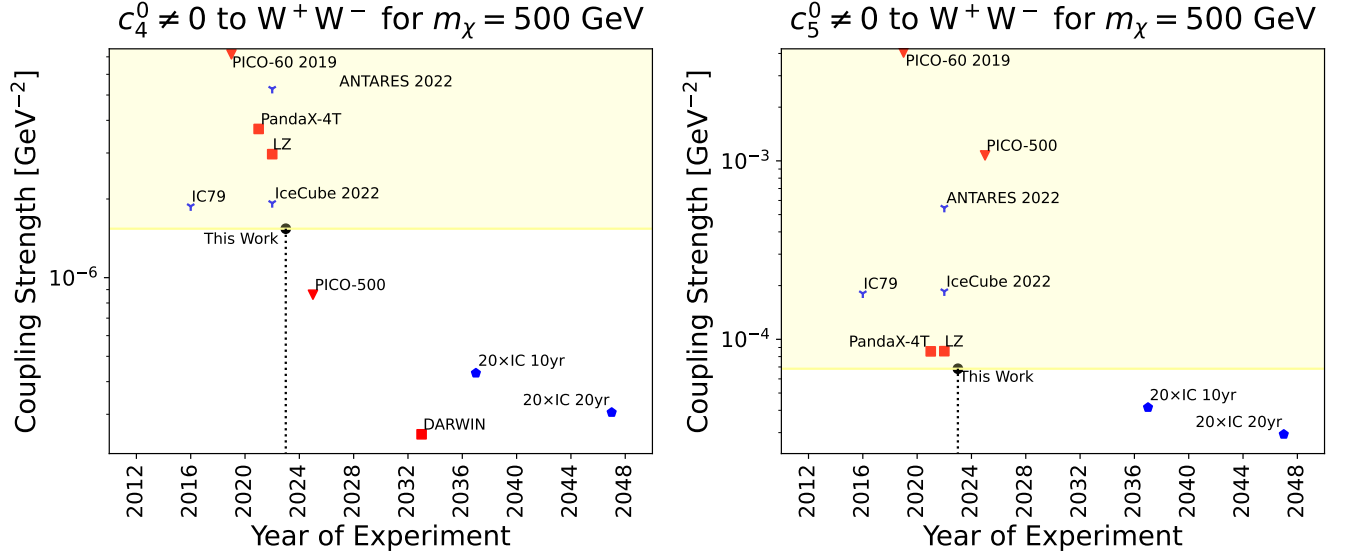
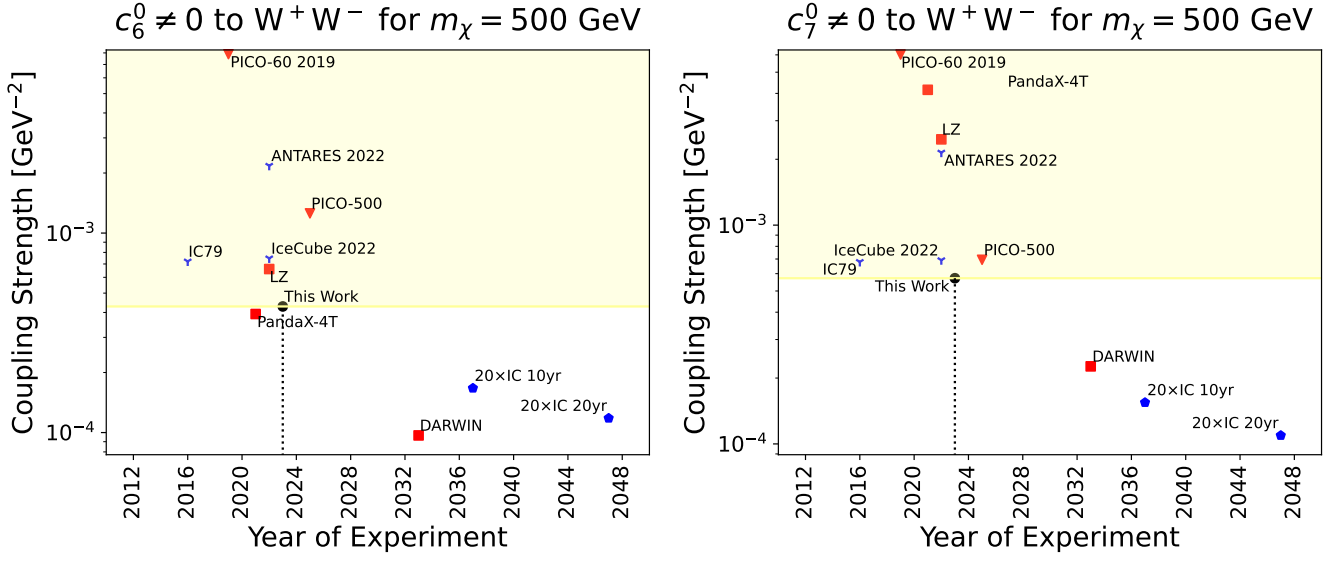
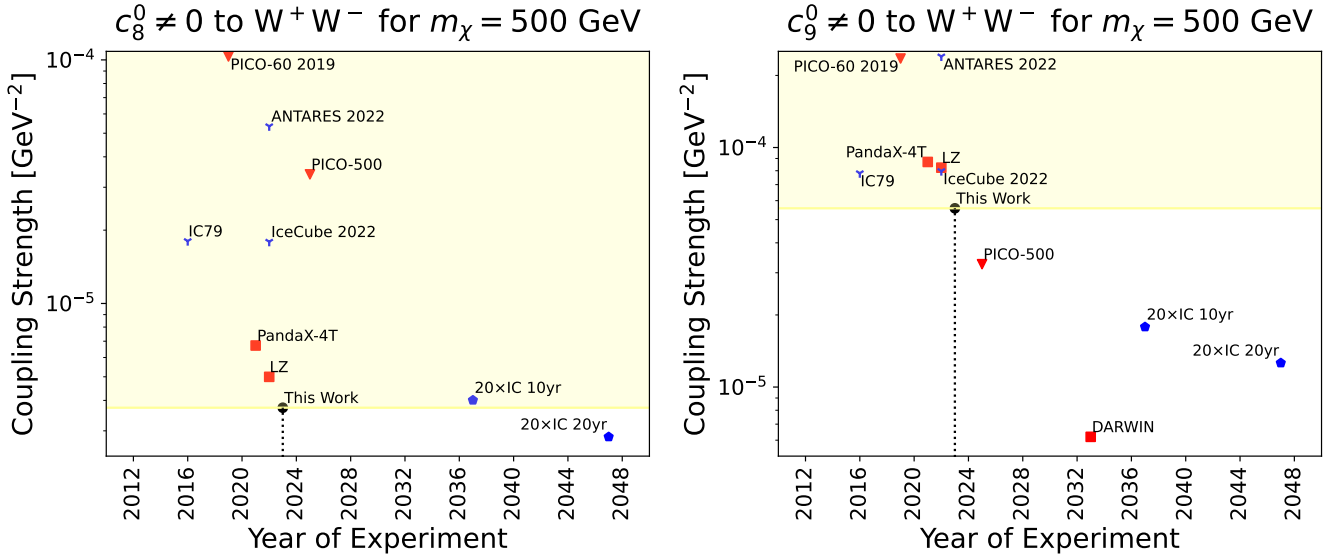


FIG. 21. The same as Fig. 20, but for c_4^0 and c_5^0 .

FIG. 22. The same as Fig. 20, but for c_6^0 and c_7^0 .FIG. 23. The same as Fig. 20, but for c_8^0 and c_9^0 .

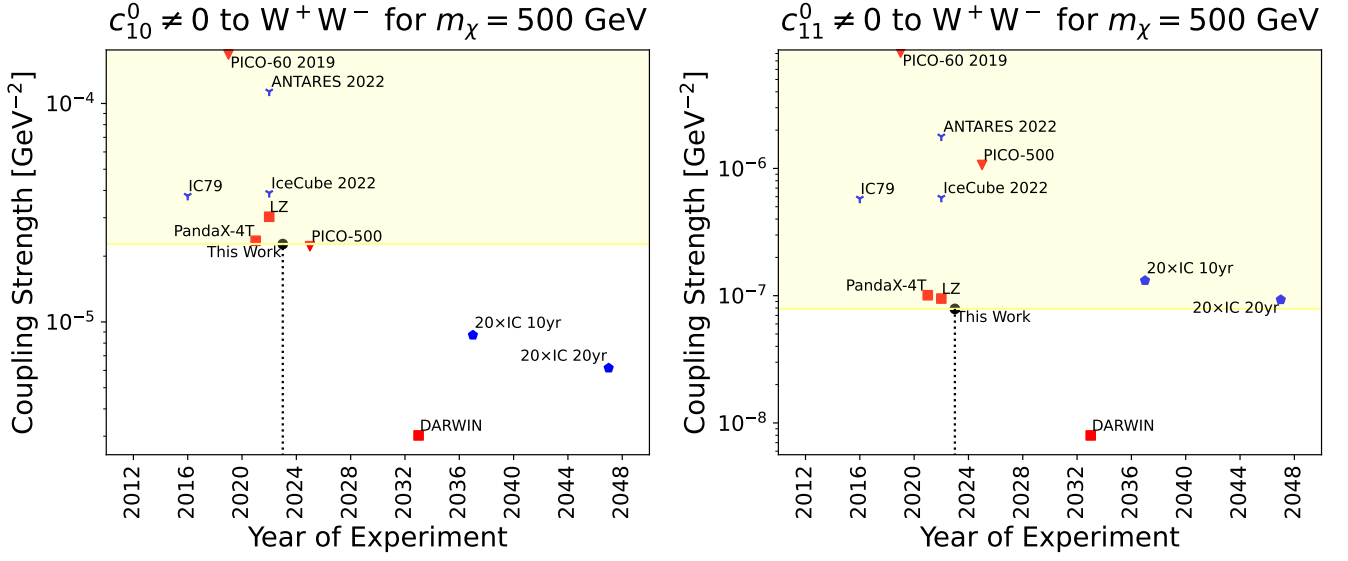


FIG. 24. The same as Fig. 20, but for c_{10}^0 and c_{11}^0 .

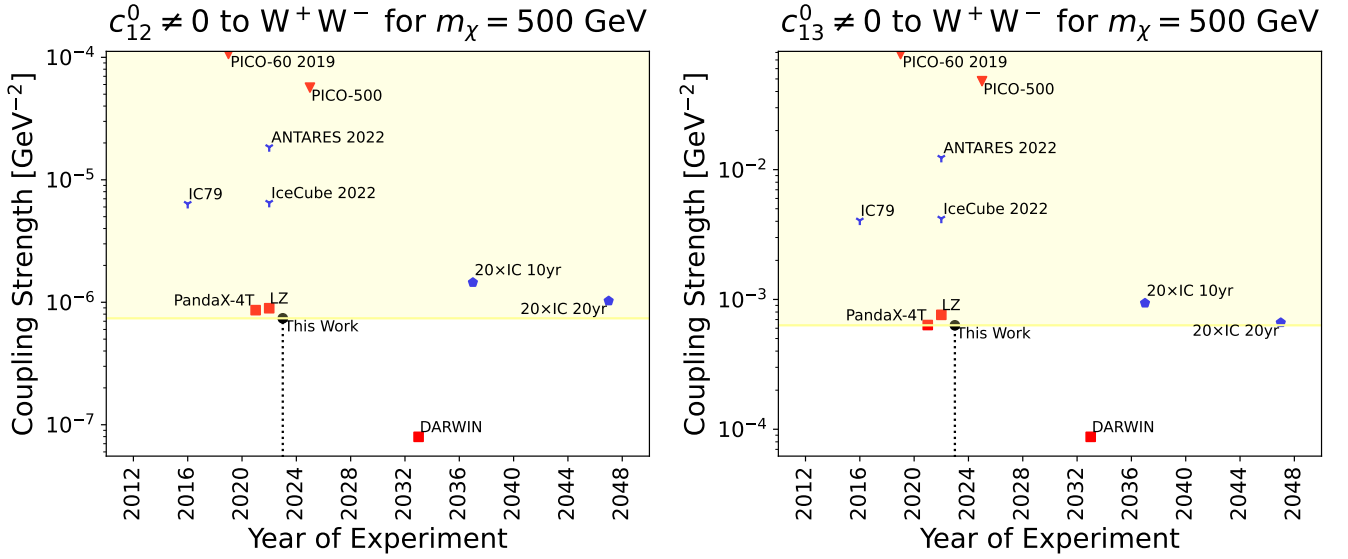


FIG. 25. The same as Fig. 20, but for c_{12}^0 and c_{13}^0 .

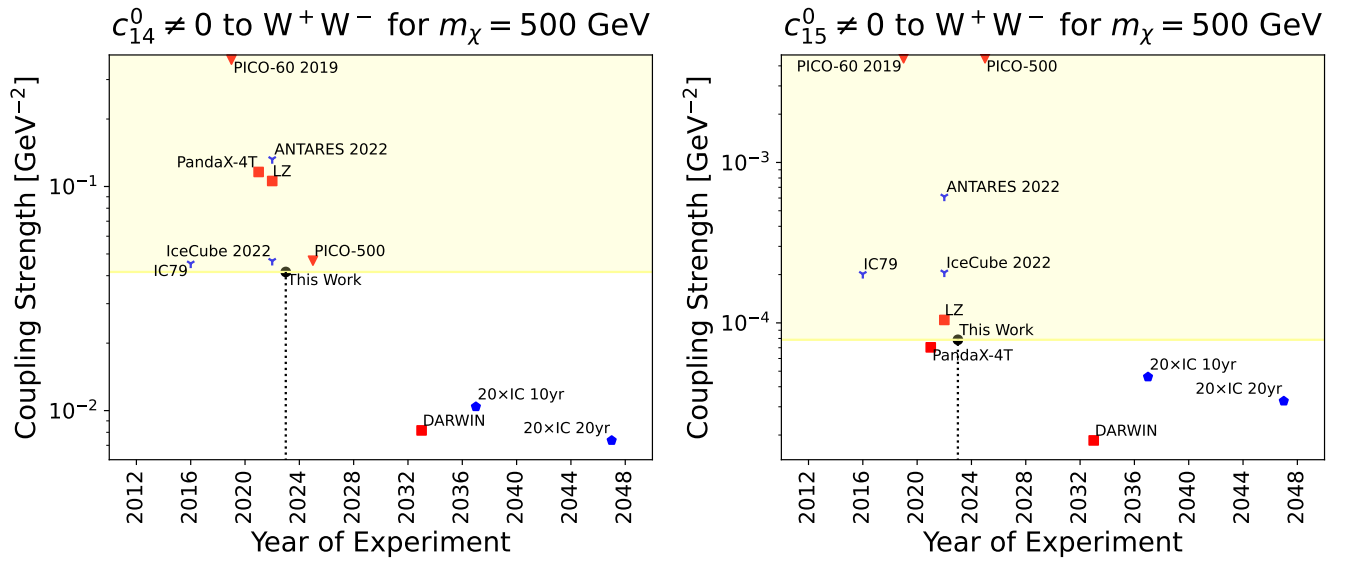


FIG. 26. The same as Fig. 20, but for c_{14}^0 and c_{15}^0 .